Supporting Information

Understanding synergistic metal–oxide interactions of in situ exsolved metal nanoparticles on pyrochlore oxide support for enhanced water splitting

Myeongjin Kim[1,], Jinho Park[2,3], Hyun Ju[2], Jin Young Kim[4], Hyun-Seok Cho[5], Chang-Hee Kim[5], Byung-Hyun Kim[6,*] and Seung Woo Lee[2,*]*

[1]Department of Hydrogen & Renewable Energy, Kyungpook National University, 80 Daehakro, Bukgu, Daegu 41566, Republic of Korea

[2]G. W. Woodruff School of Mechanical Engineering, Georgia Institute of Technology, Atlanta, GA 30332, USA

[3]Aerospace, Transportation and Advanced Systems Laboratory, Georgia Tech Research Institute, Georgia Institute of Technology, Atlanta, GA 30332, USA

[4]Fuel Cell Research Center, Korea Institute of Science and Technology (KIST), Hwarang-ro 14-gil 5, Seongbuk-gu, Seoul 02792, Republic of Korea

[5]Hydrogen Research Department, Korea Institute of Energy Research, 152 Gajeong-ro, Yuseong-gu, Daejeon 34129, Republic of Korea

[6]Platform Technology Laboratory, Korea Institute of Energy Research, 152 Gajeong-ro, Yuseong-gu, Daejeon 34129, Republic of Korea

*Corresponding authors
E-mail: Prof. Myeongjin Kim : myeongjinkim@knu.ac.kr
E-mail: Dr. Byung-Hyun Kim : bhkim@kier.re.kr
E-mail: Prof. Seung Woo Lee : seung.lee@me.gatech.edu

Experimental Methods

Preparation of PRN and PRN-X. The buffer solution was made with a mixture of a 1 M ammonia solution, 3.42×10^{-2} mol of anhydrous ethylenediaminetetraacetic acid, and 1.5 mL of nitric acid at a solution pH of 7. To synthesize $Pb_2Ru_{2-X}Ni_XO_{6.5}$ (PRN), the Ru cation precursor (0.2092 g of ruthenium(III) nitrosyl nitrate solution $[Ru(NO)(NO_3)_X(OH)_Y$, $X + Y = 3]$, Sigma-Aldrich, 1.5 wt% Ru), Ni cation precursor (0.0409 g of nickel(II) acetate tetrahydrate, $Ni(OCOCH_3)_2 \cdot 4H_2O$, Sigma-Aldrich, 99.998% trace metals basis), Pb cation precursor (0.3644 g of lead(IV) acetate, $Pb(CH_3CO_2)_4$, Sigma-Aldrich, reagent grade 95%) and 10 g anhydrous citric acid ($C_6H_8O_7$, Sigma-Aldrich, 99%) were dissolved and stirred with 500 mL of buffer solution for 24 h at 150 °C, until a gelled solution was obtained. Then, the gelled solution was dried in an oven at 200 °C for 12 h. The obtained powders were calcined and crystallized at 1300 °C for 8 h in air to produce crystalline $Pb_2Ru_{2-X}Ni_XO_{6.5}$ nanoparticles. After crystallization, the soluble compounds of the reaction mixtures were dissolved in distilled water and the solid product was centrifuged and washed repeatedly. Finally, the resulting products were dried under vacuum overnight at 60 °C to remove the remaining water. Then, 0.15 g of the obtained PRN powder was transferred into an alumina boat and reduced in a tube furnace at 450, 500, 550, and 600 °C for 5 h under 5% H_2/Ar gas flow. The reduced PRN samples are denoted as PRN-X, where X represents the reduction temperature.

Preparation of NiRu nanoalloy. The NiRu nanoalloy was prepared with following synthesis procedure: 0.039 g of Ni nanoparticles (US Research Nanomaterials, 99.9% metals basis, average particle size 20 nm) was dispersed in 10 mL of ethylene glycol ($HOCH_2CH_2OH$, Sigma-Aldrich, 99.8%) to form a homogeneous suspension by heating from 25 to 110 °C at a rate of 5 °C min^{-1} and kept at 110 °C for 20 min. Then, 10 mL of ethylene glycol dissolving 0.087 g of ruthenium(III) chloride trihydrate ($RuCl_3 \cdot 3H_2O$, Sigma-Aldrich, technical grade) was rapidly added to the above suspension, which was held at 110 °C for 3 h. Finally, the resulting products were collected by centrifugation and washed several times with methyl alcohol and distilled water, and dried under vacuum at 50 °C for 3 h.

Preparation of working electrode. To obtain the catalyst electrode, the as-synthesized PRN, PRN-450, PRN-500, PRN-550, PRN-600, Ni nanoparticle (Ni NP) (US Research Nanomaterials, 99.9%

metals basis, average particle size 20 nm), and IrO_2 (FuelCellStore, 99.9% trace metals basis, average particle size 12 nm) catalysts (7.5 mg) were mixed with 5 wt% Nafion (Sigma-Aldrich, 0.038 mL, 5 wt% in isopropanol), ethanol (0.86 mL), and deionized (DI) water (0.1 mL). The resulting slurry was ultrasonicated for 30 min to generate a catalyst ink. Then, a 4 μL amount of catalyst ink was pipetted onto the glassy carbon electrode (PINE, 5 mm diameter, 0.196 cm^2). The loading mass of catalyst on the glassy carbon electrode for PRN, PRN-450, PRN-500, PRN-550, PRN-600, Ni NP and IrO_2 is 0.207, 0.209, 0.206, 0.204, 0.205, 0.206 and 0.205 $mg_{catalyst}$ cm^{-2}, respectively. Finally, the as-prepared electrode was dried at room temperature. 20 wt% platinum on Vulcan carbon black (Pt/C) (20 wt% Pt on Vulcan XC-72R, FuelCellStore) was measured for comparison. The Pt/C catalyst ink was obtained by making the mixture of the Pt/C catalyst (5 mg) with 5 wt% Nafion (0.04 mL, in isopropanol), ethanol (1.06 mL) and DI-water (0.1 mL), then ultrasonicated for 30 min. The 11 μL of catalyst ink was pipetted onto the glassy carbon electrode (PINE, 5 mm diameter, 0.196 cm^2) and the as-prepared electrode was dried at room temperature. The loading level of 20 wt% Pt/C is 0.685 $mg_{(20\%\ Pt/C)}$ cm^{-2}, resulting in the 0.137 mg_{Pt} cm^{-2} of pure Pt.

Electrochemical measurements. The rotating disk electrode (RDE) technique was employed to measure the oxygen evolution reaction (OER) and hydrogen evolution reaction (HER) catalytic activities using a three-electrode cell setup consisting of a glassy carbon rotating disk electrode, Ag/AgCl (sat. KCl), and Pt wire as working, reference, and counter electrode, respectively, in 0.1 M KOH aqueous electrolyte. RHE calibration of the Ag/AgCl (sat. KCl) reference electrode in 0.1 M KOH was also performed (Fig. S7a). Before calibration, the 0.1 M KOH aqueous electrolyte was saturated with hydrogen by purging with ultrahigh-purity hydrogen gas (99.999%) for 30 min. The calibration was conducted in H_2-saturated 0.1 M KOH electrolyte, with a Pt RDE as a working electrode. Forward and reverse cyclic voltammetry (CV) scans were performed at a scan rate of 1 mV s^{-1} and the average of the two potentials corresponding to zero current was taken as the thermodynamic potential for the hydrogen electrode reactions. Before investigating the OER and HER activity of the as-prepared electrocatalysts by RDE experiments, the 0.1 M KOH aqueous electrolyte was saturated with oxygen by purging with ultrahigh-purity oxygen gas (99.995%) and saturated with nitrogen by purging with

ultrahigh-purity nitrogen gas (99.999%) for 30 min, respectively. Linear sweep voltammetry (LSV) curves were recorded on the RDE at a scan rate of 5 mV s^{-1} and 1600 rpm in O_2-saturated (for OER) and N_2-saturated (for HER) 0.1 M KOH solution. All potential values were *iR*-corrected (Figs. S7b and S18) to compensate for the effect of the solution resistance, using the following equation:

$$E_{iR-corrected} = E - iR \quad (1)$$

where *i* is the current and *R* is the uncompensated Ohmic resistance of the electrolyte (~ 43 Ω) measured by high-frequency AC impedance in 0.1 M KOH (Figs. S10 and S22). Electrochemical impedance spectroscopy (EIS) measurements were recorded from 100 kHz to 0.1 Hz with an amplitude of 10 mV.

Characterization methods. X-ray diffraction (XRD, New D8-Advance, Bruker-AXS) patterns were collected at a scan rate of 1° s^{-1} within the 2θ range of 10°–80° and using Cu $K_{\alpha 1}$ radiation (0.154056 nm). The morphologies of the samples were analyzed using high-resolution transmission electron microscopy (HR-TEM, JEM-2100F, JEOL) at 200 kV. Scanning transmission electron microscopy (STEM) characterization was conducted utilizing a probe-corrected JEOL ARM-200F instrument at 200 kV, equipped with an energy dispersive X-ray (EDX) detector. X-ray photoelectron spectroscopy (XPS) analysis was performed on a PHI 5000 VersaProbe II (Japan) with a monochromatic Al Kα (hv = 1486.69 eV) X-ray source. X-ray absorption spectroscopy (XAS) measurements were performed on the BL7D beamline at the Pohang Light Source (PLS), operating in top-up mode under a ring current of 300 mA at 3.0 GeV. The incident beam was collimated by a Ru-coated mirror at 2.8 mrad and monochromatized using a channel-cut Si (1 1 1) monochromator. The acquired extended X-ray absorption fine structure (EXAFS) data were processed according to standard procedures using the ATHENA module implemented in the IFEFFIT software packages. The EXAFS spectra were obtained by subtracting the post-edge background from the overall absorption and then normalizing it with respect to the edge-jump step. Subsequently, the χ(k) data in k-space were Fourier-transformed to real (R) space using a Hanning window to separate the EXAFS contributions from different coordination shells. *Operando* XAS analysis was conducted using an in-house developed three-electrode configuration consisting of an as-prepared electrocatalyst-based air electrode, Ag/AgCl (KCl Sat.) and Pt wire as working, reference, and counter electrode, respectively, in 0.1 M KOH aqueous electrolyte.

Briefly, X-ray photons entered the air electrode through the backside of it, and fluorescent photons exiting the electrode were detected at 90 degrees relative to the incident beam. This makes it possible to collect the XAS spectra of the catalysts during the electrochemical process. For the electrocatalyst-based air electrode fabrication, glassy carbon plates were used as working electrodes, serving as substrates for the catalysts. The as-prepared catalysts ink was dropped on the plates and fully dried. Then the working electrode was attached to the cells with fast-curing epoxy (Devcon). Conductive Cu tape was linked to the backside of the working electrode to make the electrical connection. *Operando* XAS measurements were carried out in top-up mode under a ring current of 300 mA at 3.0 GeV and recorded between 1.44 and 1.49 V vs. RHE for OER and between -0.005 and -0.379 V vs. RHE for HER, and the applied potential was stabilized for 5 min before XAS experiments, respectively. Temperature-programmed reduction (TPR) analysis of the catalysts was conducted in an AMI 200 (Altamira Instruments, Pittsburgh, PA) fixed-bed reactor. For each run, 100 mg of catalyst was loaded into a 0.25-inch quartz tube. Before starting the TPR measurements, the samples were treated with O_2 to remove any surface impurities left from the synthesis. For this treatment, each sample was heated from ambient temperature to 850 °C at a rate of 10 °C min^{-1} in 5% O_2/He, with a flow rate of 20 mL min^{-1}. The sample was then purged with pure He at a flow rate of 20 mL min^{-1} for 15 min and then cooled to room temperature in He. Next, the sample was exposed to a mixture of 5% H_2/Ar flowing at 30 mL min^{-1}, increasing the temperature from 50 to 850 °C at 10 °C min^{-1}. After that, the sample was held at 850 °C for 30 min and then cooled to room temperature. The H_2 consumption was monitored using a thermal conductivity detector.

Computational Methods. The spin-polarized density functional theory (DFT) calculations were performed using the Vienna ab-initio simulation package (VASP).[1-4] The projector augmented wave (PAW) method[5, 6] was used to describe the interaction between core and valence electrons, explicitly treating the H $1s^1$, O $2s^2 2p^4$, Pb $6s^2 6p^2$, Ni $3d^8 4s^2$, Ru $4d^7 5s^1$ electrons. The exchange-correlation energy was described by the Perdew-Burke-Ernzerhof (PBE) functional within the generalized gradient approximation (GGA).[7] The Kohn-Sham single-electron wave functions were expanded with a basis set of plane waves with kinetic energies up to 500 eV. The convergence criterion for total electronic energy

was set to be 10^{-6} eV. Geometry optimizations for all model structures were carried out until the maximal force acting on each atom became less than 0.02 eV/Å. The Brillouin zone was sampled using the Monkhorst-Pack scheme[8] with 3×3×1 *k*-points for metal slabs and 2×2×1 *k*-points for pyrochlore oxide slabs or metal/oxide interface systems. To describe the Ni and NiRu nanoparticles, a slab model structure with 5 layers exposing the (111) crystal plane was used. The bottom 2 layers were fixed to mimic a bulk system while the other 3 layers were allowed to fully relax. Since the XRD measurement revealed that the crystal structure of the exsolved NiRu nanoalloys is a *fcc* structure which is almost identical to that of Ni nanoparticles with a slight shift (Fig. S4 and S5), the atomistic model structure for both Ni and NiRu was constructed based on a Ni *fcc* structure. For NiRu nanoalloys, two different slab models were prepared depending on the location of a Ru layer: one has a Ru layer covering Ni slabs, referred to as "NiRu-Ru_{top}" while the other has a Ru layer located below the top surface of Ni, referred to as "NiRu-Ru_{2nd}" (Fig. 4d-i in the main article). Additional two random model structures (NiRu-Ru_{rand1} and NiRu-Ru_{rand2}) for NiRu alloys where Ru is randomly substituted with Ni within the top two layers (Fig. S30) were also prepared. Metal/oxide interface systems were composed of 3 layers of Ni(NiRu) and 3 layers of a Pb-Ru-O or Pb-O bundle. The lateral size and rotation of the metal/oxide systems perpendicular to the interface plane were determined by minimizing the lateral strain caused by lattice mismatch. For example, our model structure of Ni/$Pb_2Ru_2O_{6.5}$ exhibits –2.07% for both ε_{xx} and ε_{yy} while that of Ni/PbO shows 1.12 % and 1.20 % for ε_{xx} and ε_{yy}, respectively. Here, the tensile (compressive) strain is represented with positive (negative) values. The optimized lattice constant for the oxide supports was fixed while strain was imposed on the metal layers. For NiRu/$Pb_2Ru_2O_{6.5}$ and NiRu/PbO structures, the location of a Ru layer was also varied in the NiRu layers as shown in Fig. S29. We use the label "NiRu-Ru_{top}/$Pb_2Ru_2O_{6.5}$" to refer to the NiRu/$Pb_2Ru_2O_{6.5}$ structure in which a layer of Ru is located on the surface of NiRu layers. Similarly, the labels "NiRu-Ru_{mid}/$Pb_2Ru_2O_{6.5}$" and "NiRu-Ru_{btm}/$Pb_2Ru_2O_{6.5}$" were used according to the location of a Ru layer. The model structures of PRN were constructed by substituting Ni with Ru. Here it should be mentioned that the composition of Ni for the DFT calculates was chosen as 0.333 although the experimental value is 0.4 due to the limitation of cell size. All the atoms were fully relaxed except atoms at the bottommost

layer. For all the model structures, a vacuum region of 15 Å along the z-axis normal to the surface, which is large enough to minimize the image-image interactions, was introduced.

We used the Gibbs free energy of the H adsorption as a descriptor to determine the HER activity. The H adsorption energy was calculated from the following equation:

$$\Delta E_{\mathrm{H}} = E_{\mathrm{H}*} - (E_{*} + 1/2E_{\mathrm{H_2}}) \quad \text{S(1)}$$

where * denotes a clean slab, thus E_{*}, $E_{\mathrm{H}*}$ and $E_{\mathrm{H_2}}$ are the total energy of a clean surface, a H adsorbed surface, and a molecular H_2, respectively. The Gibbs free energy of the adsorbed state was then calculated from the following equation:

$$\Delta G_{\mathrm{H}*} = \Delta E_{\mathrm{H}} + \Delta E_{ZPE} - T\Delta S_{\mathrm{H}} \quad \text{S(2)}$$

where ΔE_{ZPE} is the difference in zero point energy between the adsorbed H and the gas phase and $\mathrm{T}\Delta S_{\mathrm{H}}$ is the entropic contribution to the free energy. The values for ΔE_{ZPE} and $\mathrm{T}\Delta S_{\mathrm{H}}$ were taken from the Nørskov's work[9] leading to $\Delta G_{\mathrm{H}*} = \Delta E_{\mathrm{H}} + 0.24$ at 300 K. The hollow-fcc site was chosen as an adsorption site for a hydrogen atom because hydrogen energetically prefers to bind with Ni atoms at this site. For the sake of fair comparison, this adsorption site was also used for the NiRu nanoalloys. The Bader charge analysis was performed using the work proposed by Henkelman et al.[10] The O 2p band center was defined as the weighted average energy of the density of states (DOS) projected on the 2p states of O atoms in the pyrochlore oxide relative to the Fermi level as described by Dickens et al.[11] For the water dissociation calculations, the geometry optimized atomic configurations of the H_2O adsorption and dissociation on the pyrochlore oxide $Pb_2Ru_2O_{6.5}$(111), Ni(111), NiRu-Ru_{top}(111) and NiRu-Ru_{2nd}(111) were selected as the initial (reactant) and final (product) states. The climbing image nudged elastic band method (CI-NEB) proposed by G. Henkelman[12, 13] was applied to identify the transition state of the water dissociation. Four and six intermediate images along the minimum energy path were used for metal and oxide slabs, respectively. All the configurations were relaxed until the maximal force acting on each atom becomes less than 0.1 eV/Å with a spring constant between each image of -5.0 eV/Å^2.

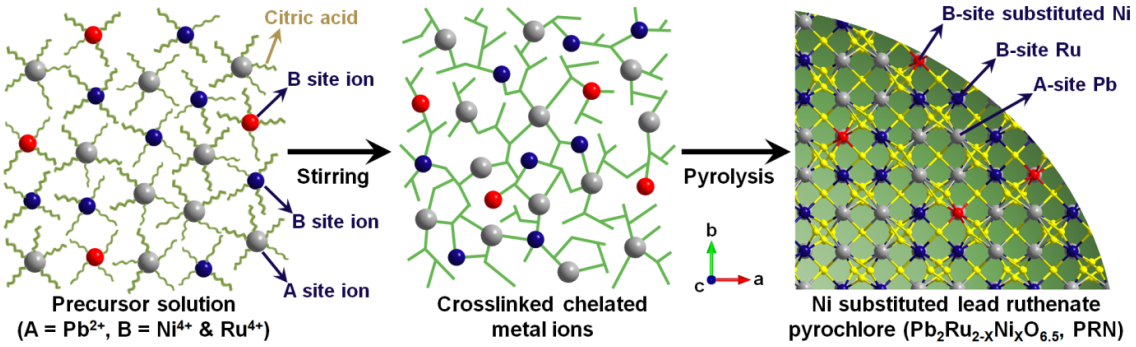

Fig. S1. Schematic illustration of the preparation of Ni-substituted lead ruthenate pyrochlore oxide ($Pb_2Ru_{2-X}Ni_XO_{6.5}$, PRN). The PRN was synthesized *via* a sol-gel method using the uniformly cross-linked A and B-site metal cations with citric acid as a chelating agent. The prepared cross-linked precursor particles were crystallized at 1300 °C to generate crystalline Ni-substituted lead ruthenate pyrochlore oxide nanoparticles.

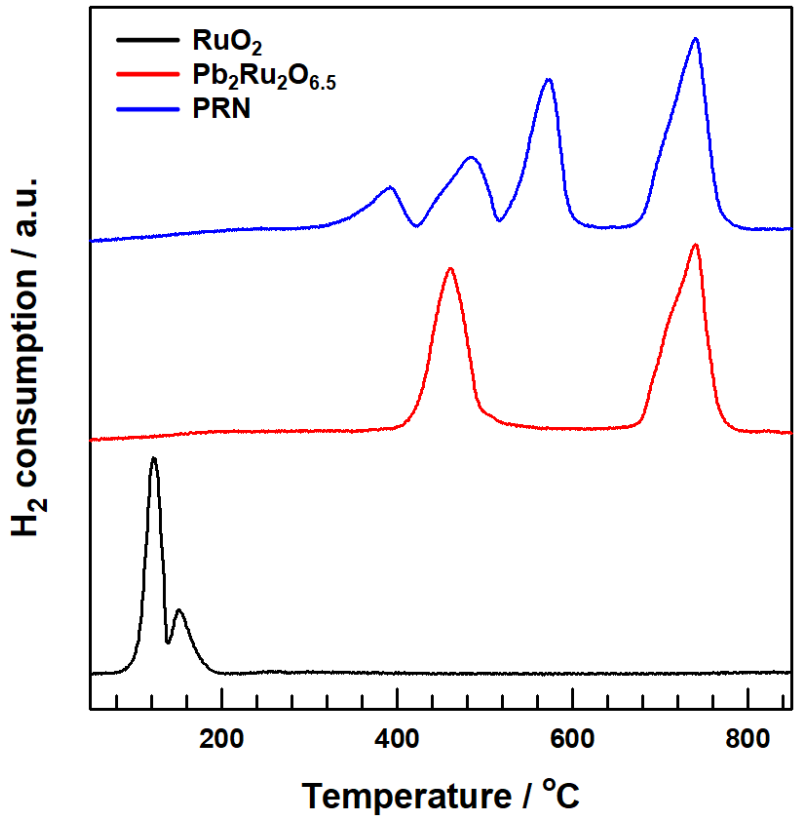

Fig. S2. Temperature-programmed reduction (TPR) profiles of RuO_2, $Pb_2Ru_2O_{6.5}$, and PRN. The TPR profile of RuO_2 exhibited two reduction peaks at 124 and 148 °C, which were ascribed to the reduction of Ru cations in RuO_2.[14] The TPR profile of $Pb_2Ru_2O_{6.5}$ showed the reduction peak of Ru at a significantly increased temperature of 460 °C, along with the reduction peak of Pb at 740 °C. When Ru cations occupy the B-sites of the metallic pyrochlore oxide structure, the B-site Ru forms a rigid RuO_6 octahedral structure, which can significantly enhance the stability of the Ru species in a reducing environment.[15] The TPR profile PRN displayed two reduction peaks at 390 and 480 °C, associated with the reduction of Ni^{3+} to Ni^{2+} and of Ni^{2+} to Ni^0, respectively. Importantly, the reduction peak of Ru cations was shifted to 570 °C, due to the decreased amount of surface Ru atoms after the B-site substitution of Ni cations.[16] As a result, the Ni cations of PRN were reduced to metallic Ni and deposited on the surface of PRN in the reduction temperature range of 430-510 °C. At the same time, some of the Ru cations were also reduced to metallic Ru, leading to the formation of the NiRu nanoalloy above 520 °C.

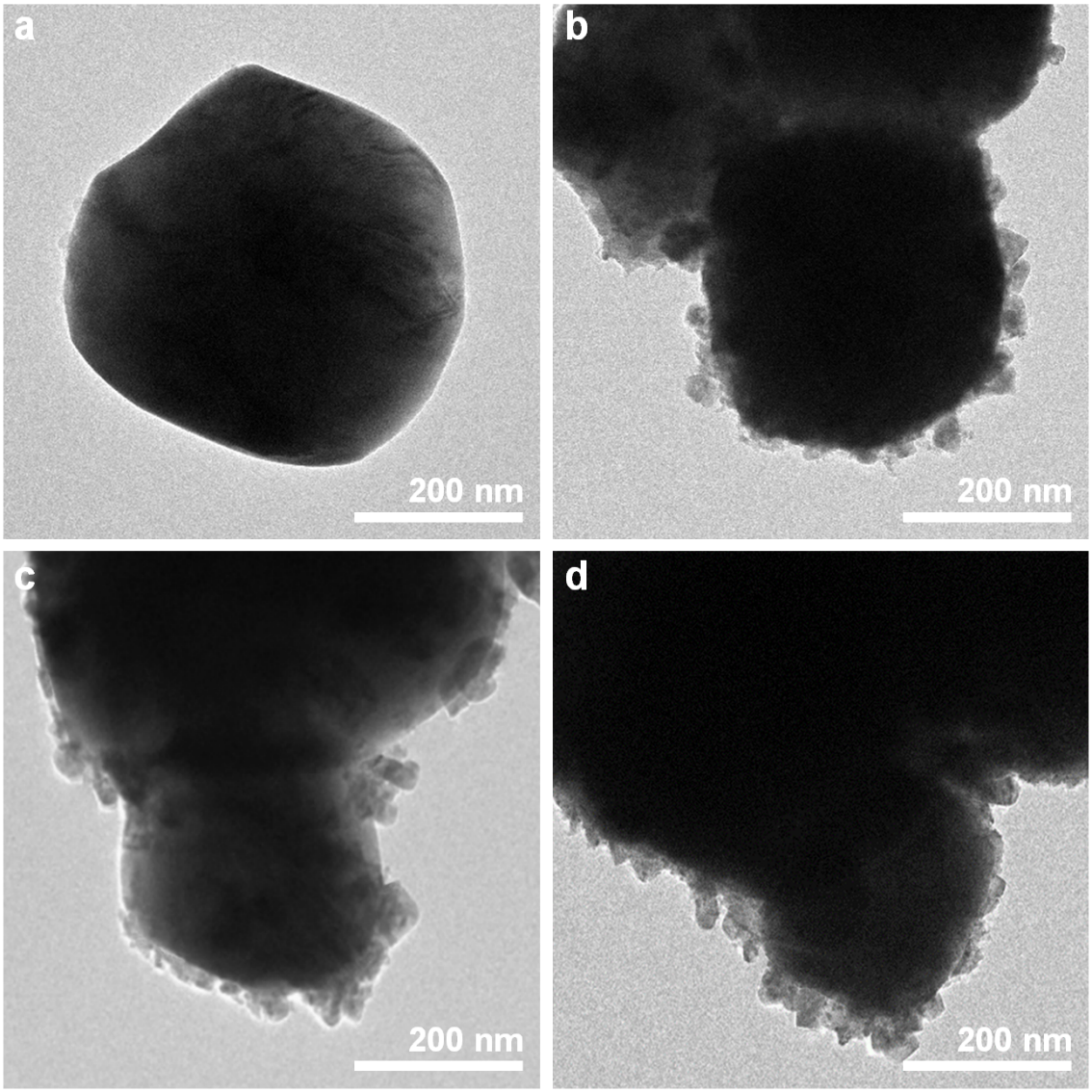

Fig. S3. Low-magnification HR-TEM image of (a) PRN, (b) PRN-500, (c) PRN-550 and (d) PRN-600.

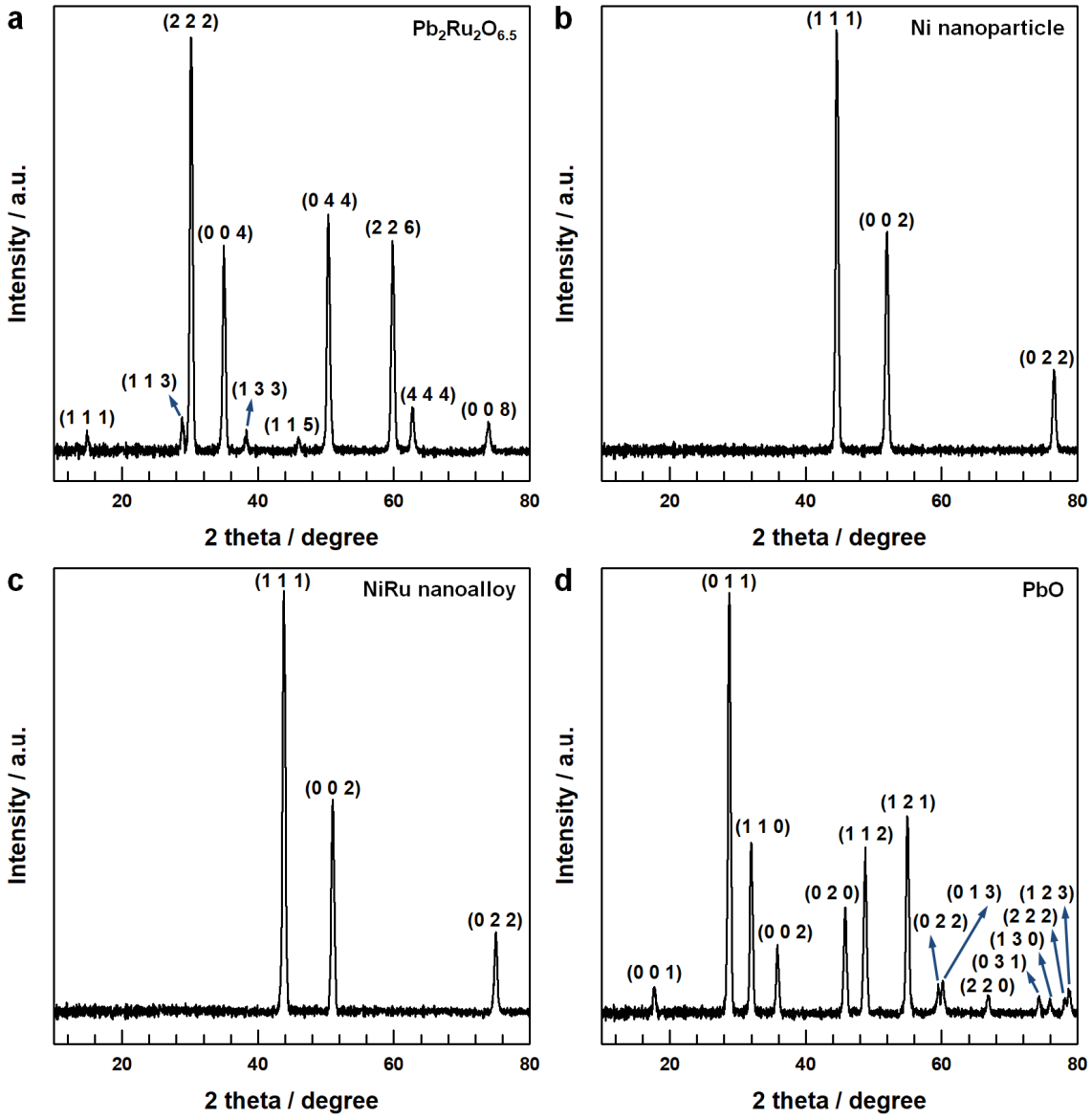

Fig. S4. X-ray diffraction (XRD) patterns of (a) $Pb_2Ru_2O_{6.5}$, (b) Ni nanoparticle, (c) NiRu nanoalloy, and (d) PbO. The XRD pattern of $Pb_2Ru_2O_{6.5}$ could be indexed to a typical cubic structure with $Fd\bar{3}m$ space group.[17, 18] Moreover, although both metallic Ni nanoparticle and NiRu nanoalloy exhibit the (1 1 1), (0 0 2) and (0 2 2) crystalline planes, these diffraction peaks were slightly shifted to lower diffraction angle when forming the NiRu nanoalloy.

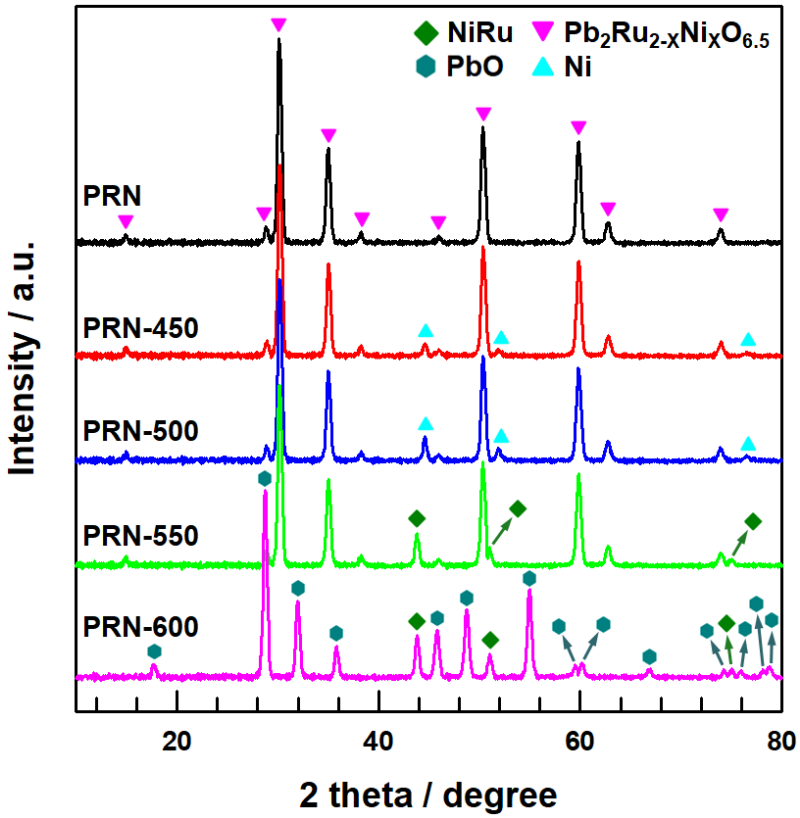

Fig. S5. XRD patterns of PRN, PRN-450, PRN-500, PRN-550 and PRN-600. Both PRN and $Pb_2Ru_2O_{6.5}$ exhibit the typical cubic structure by similar XRD patterns with Fd-3m space group, indicating the Ni cations were successfully substituted at B-site $Pb_2Ru_2O_{6.5}$ pyrochlore oxide without phase transformation.[17, 18] At the reduction temperature of 450 °C, the Ni cations substituted for the B-site began to be reduced to the metallic phase, and metallic Ni was simultaneously extracted to the PRN surface, giving rise to Ni nanoparticles.[19] Accordingly, diffraction peaks corresponding to the metallic Ni phase appeared for PRN-450; these peaks were further enhanced for PRN-500, due to the appearance of more metallic Ni nanoparticles at higher temperatures. When the reduction temperature was further increased to 550 °C, the metallic Ni peaks slightly shifted to lower diffraction angles, closely matching the diffraction peaks of the NiRu alloy (Fig. S4c). This indicates that the B-site Ru cations were reduced to the metallic Ru phase and began to form a nanoalloy with Ni on the PRN surface at high temperature (550 °C). Importantly, the XRD patterns of PRN-450, PRN-500 and PRN-550 products displayed the diffraction peaks of $Pb_2Ru_2O_{6.5}$, confirming that the cubic crystal pyrochlore oxide structure was well retained during the thermal exsolution process. However, XRD pattern of PRN-600 shows the

diffraction peaks attributed from $Pb_2Ru_2O_{6.5}$ are perfectly transformed to tetragonal PbO phase (Fig. S4d) because the reduction of all Ru cations in B-site causes the collapse of pyrochlore oxide crystal structure.[20]

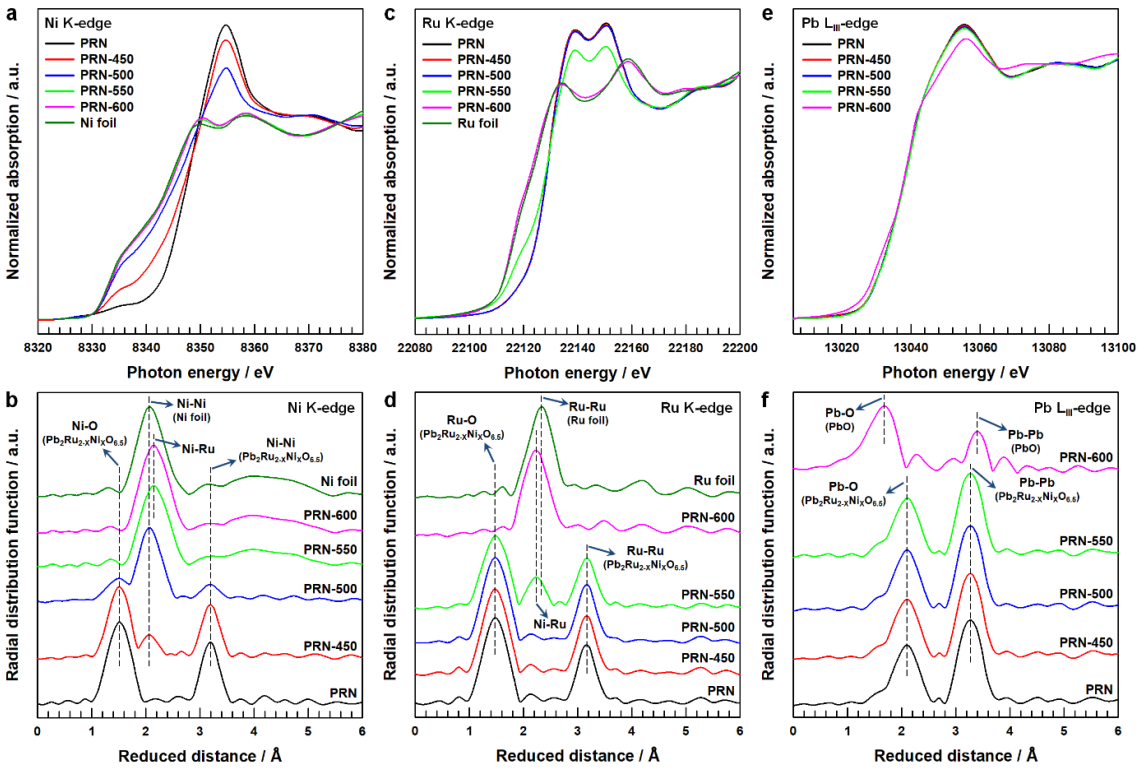

Fig. S6. (a,b) Ni K-edge XANES and EXAFS spectra of PRN, PRN-X, and reference Ni foil. (c,d) Ru K-edge XANES and EXAFS spectra of PRN, PRN-X, and reference Ru foil. (e,f) Pb L_{III}-edge XANES and EXAFS spectra of PRN and PRN-X. The structural changes taking place in PRN during the thermal reduction process were investigated in detail using XAS measurements. The Ni K-edge X-ray absorption near-edge structure (XANES) spectrum of PRN showed a strong signal at a photon energy of 8354 eV, which was ascribed to the Ni cations substituted at B-sites (Fig. S6a). The intense white line at 8354 eV decreased for PRN-450 and PRN-500, along with the appearance of the metallic Ni signal at 8335 eV.[21] When PRN was further reduced at 550 and 600 °C, the intense white line disappeared, and the spectrum closely matched that of Ni foil. This reveals that the Ni cations substituted in PRN were fully reduced to metallic Ni at such high reduction temperatures. The Fourier-transformed (FT) extended X-ray absorption fine structure (EXAFS) Ni K-edge spectrum of PRN exhibited two peaks at the reduced distances of 1.51 and 3.19 Å, respectively, corresponding to Ni-O and Ni-Ni bonds at the B-sites of the pyrochlore oxide structure (Fig. S6b). PRN-450 exhibited a new peak at a reduced distance of 2.06 Å, associated with metallic Ni-Ni bond, which also can be observed in the spectrum of Ni foil.[22] The EXAFS spectrum of PRN-500 showed a significantly stronger peak

corresponding to metallic Ni-Ni bonds, but also displayed the reduced intensity of Ni-O and Ni-Ni bond peaks at the B-site. This indicates that a large portion of the Ni cations substituted in the B-site were reduced to metallic Ni. For PRN-550 and PRN-600, the Ni-O and Ni-Ni bond peaks of the pyrochlore oxide completely disappeared and the metallic Ni-Ni peak slightly shifted to a longer reduced distance, due to the alloying of Ni and Ru. The Ru K-edge XANES spectrum of PRN exhibited two peaks at 22139 and 22150 eV, induced by the dipole-allowed transition from Ru 1s to the bound 5p and continuum 5p states, respectively (Fig. S6c).[17] The XANES spectra of PRN-450 and PRN-500 overlapped with that of PRN, indicating negligible changes in the local geometric and electronic structure of Ru cations. However, the peak intensities at 22139 and 22150 eV considerably decreased in the XANES spectrum of PRN-550, along with the appearance of the metallic Ru signal at 22118 eV.[23] This indicates that at 550 °C, the Ru cations at the B-site were partially reduced to the metallic Ru phase. At a higher temperature of 600 °C, the metallic Ru signal is close to Ru foil and these split maximum peaks are also transformed to metallic Ru foil, indicating that the B-site Ru cations were perfectly reduced and existed as the metallic phase in PRN-600. PRN, PRN-450, and PRN-500 displayed similar Ru K-edge EXAFS spectra, showing two peaks at reduced distances of 1.47 and 3.18 Å corresponding to the Ru-O and Ru-Ru bonds at B-sites, respectively (Fig. S6d). On the other hand, for PRN-550, a new Ni-Ru alloy peak appeared at a reduced distance of 2.24 Å, slightly lower than that of the metallic Ru-Ru peak (2.32 Å) with the decreased intensities of Ru-O and Ru-Ru bond peaks from B-site, indicating the formation of the NiRu nanoalloy. For PRN-600, the Ru-O and Ru-Ru bond peaks from pyrochlore oxide structure disappeared, indicating that all Ru cations in pyrochlore oxide were reduced to the metallic phase. PRN, PRN-450, PRN-500 and PRN-550 displayed similar Pb L_{III}-edge XANES and EXAFS spectra with A-site pyrochlore oxide, but for PRN-600, the Pb-O and Pb-Pb bond peaks were converted to tetragonal PbO (Figs. S6e and f).[24] These results confirm that the crystal structure of pyrochlore oxide support was transformed to PbO at 600 °C due to the exsolution of all Ru cations, which is consistent with XRD results (Fig. S5).

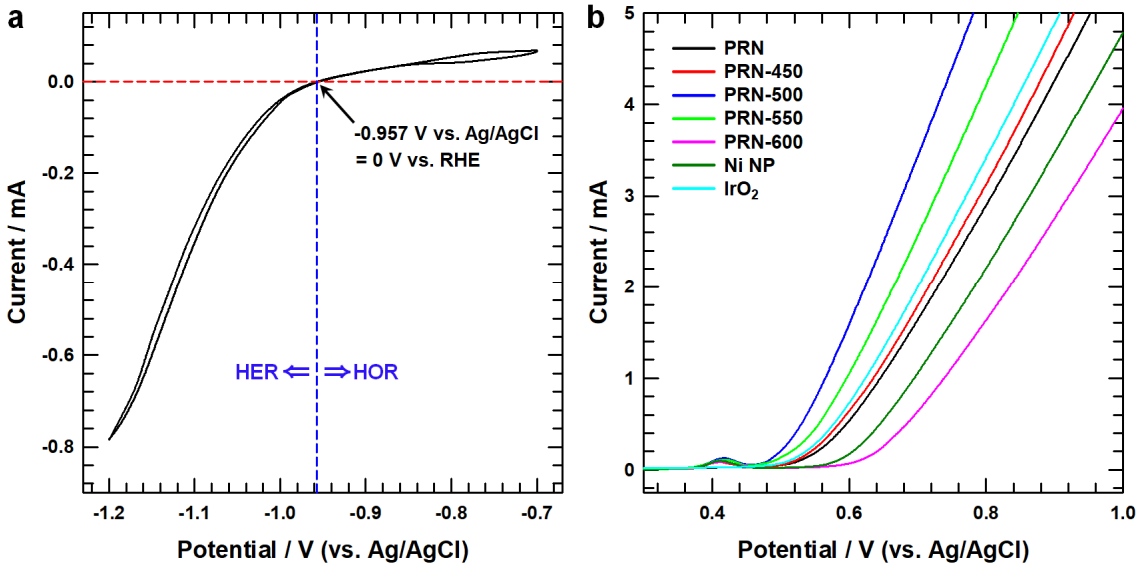

Fig. S7. (a) RHE calibration of the Ag/AgCl reference electrode in 0.1 KOH solution. The thermodynamic potential for the hydrogen electrode reactions was determined by averaging the two potentials corresponding to zero current in forward and reverse CV scans at a scan rate of 1 mV s^{-1}. (b) OER polarization curves without RHE calibration and *iR* correction for PRN, PRN-X, Ni NP and IrO_2 benchmark, measured on a RDE at a scan rate of 5 mV s^{-1} and 1600 rpm in O_2-saturated 0.1 M KOH electrolyte.

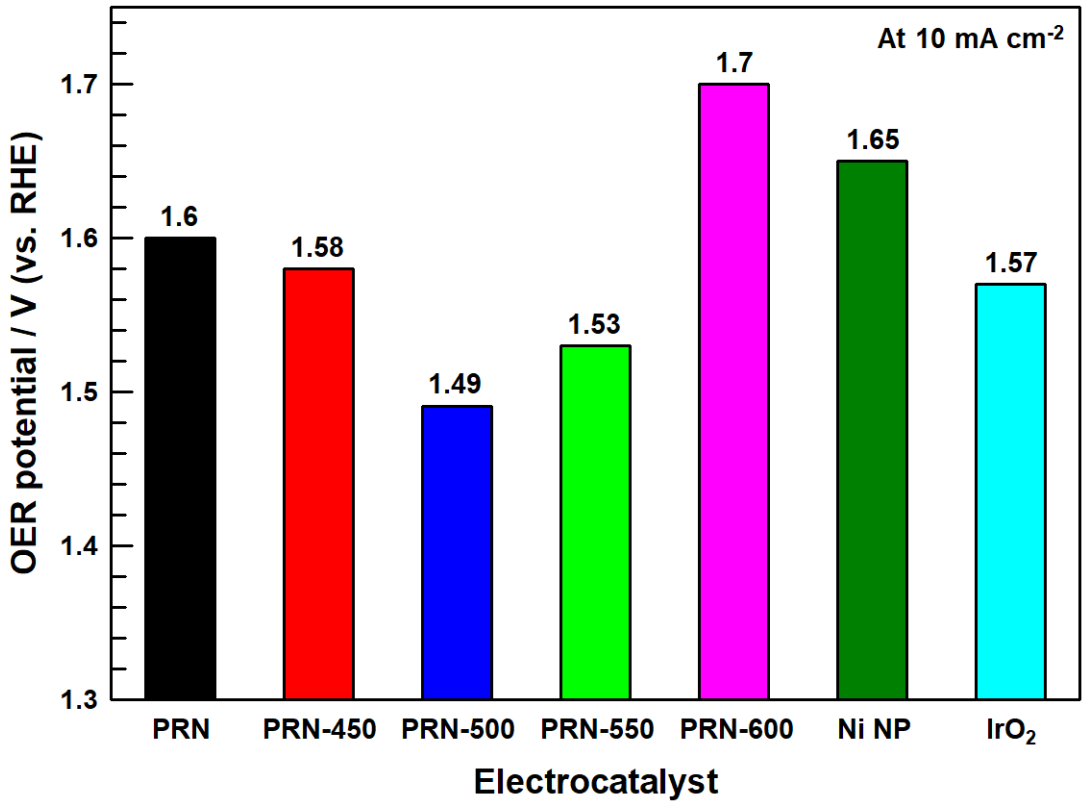

Fig. S8. Comparison of the OER potentials required to achieve a current density of 10 mA cm^{-2} for PRN, PRN-X, Ni NP and IrO_2 benchmark.

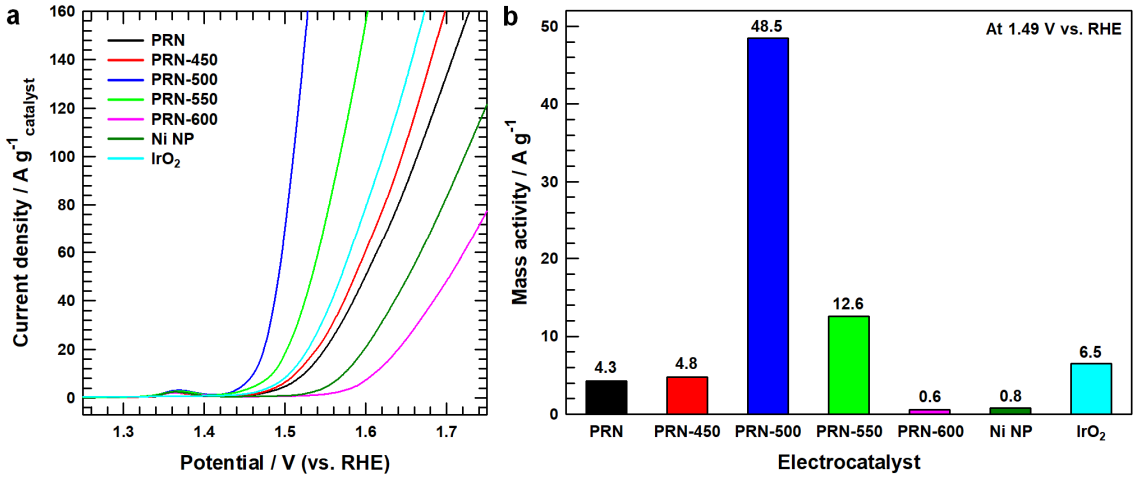

Fig. S9. (a) OER polarization curves normalized to catalyst mass for PRN, PRN-X, Ni NP and IrO_2, measured at a scan rate of 5 mV s^{-1} and 1600 rpm in O_2-saturated 0.1 M KOH electrolyte. (b) Mass activity of PRN, PRN-X, Ni NP and IrO_2 benchmark at 1.49 V vs. RHE. The LSV curves normalized by the loading mass of electrocatalyst exhibited a similar trend to that of the LSV curves based on the RDE electrode area. PRN-500 delivered the highest mass activity of 48.5 A g^{-1} at a potential of 1.49 V vs. RHE, which was 11.3 and 7.4 times higher than that of PRN (4.3 A g^{-1}) and IrO_2 (6.5 A g^{-1}), respectively.

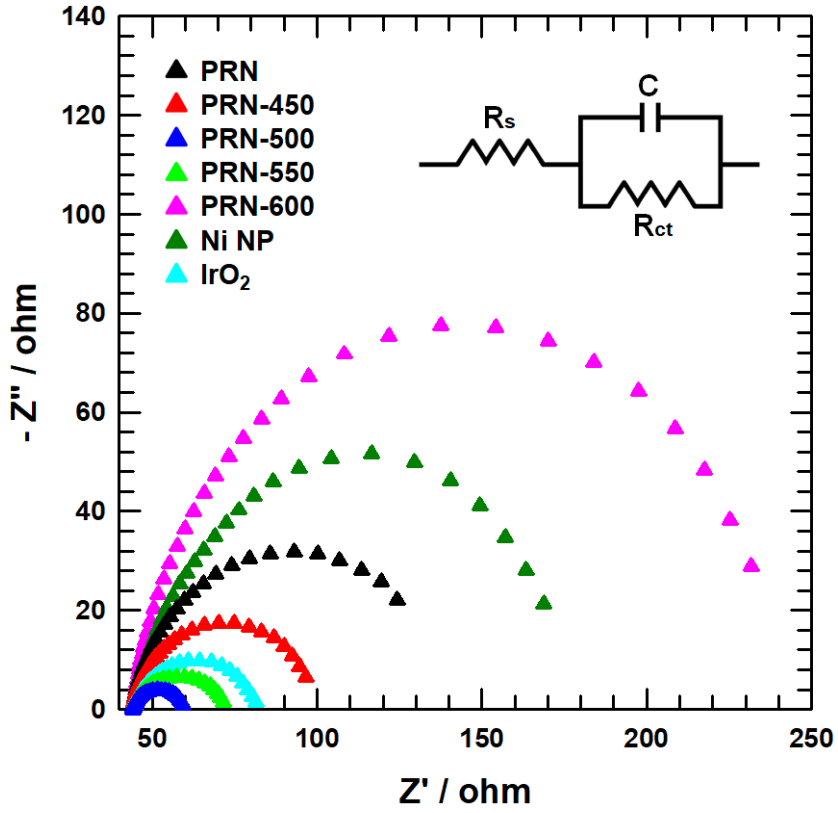

Fig. S10. Nyquist plots for PRN, PRN-X, Ni NP and IrO_2 recorded at 1.49 V vs. RHE. The Tafel slopes and charge transfer resistances (R_{ct}) obtained from the Tafel and Nyquist plots (Fig. 2b and Fig. S10, respectively) varied in the order PRN-600 (238 mV dec^{-1}, 187.549 Ω) > Ni NP (157 mV dec^{-1}, 124.657 Ω) > PRN (142 mV dec^{-1}, 80.107 Ω) > PRN-450 (122 mV dec^{-1}, 52.361 Ω) > IrO_2 (83 mV dec^{-1}, 37.218 Ω) > PRN-550 (67 mV dec^{-1}, 27.415 Ω) > PRN-500 (43 mV dec^{-1}, 15.174 Ω), further confirming the fast oxygen evolution kinetics of PRN-500.

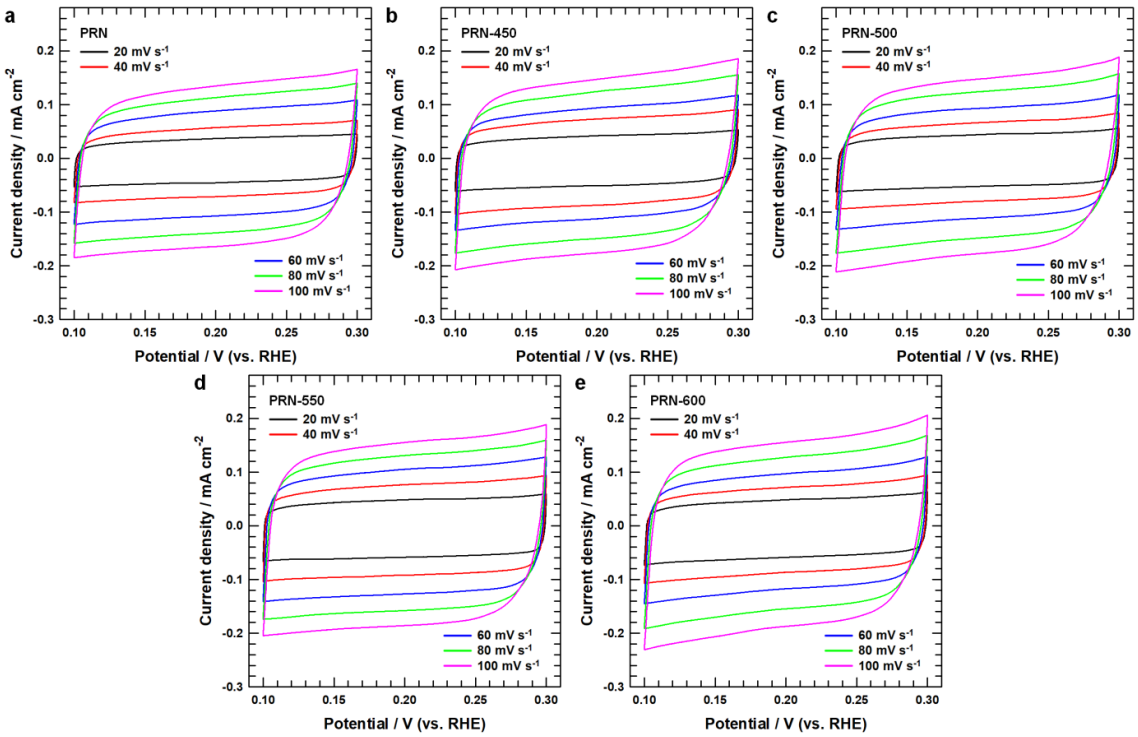

Fig. S11. CV scans of (a) PRN, (b) PRN-450, (c) PRN-500, (d) PRN-550 and (e) PRN-600 in a non-faradic current region (0.1 – 0.3 V vs. RHE) at different scan rates of 20, 40, 60, 80 and 100 mV s^{-1}.

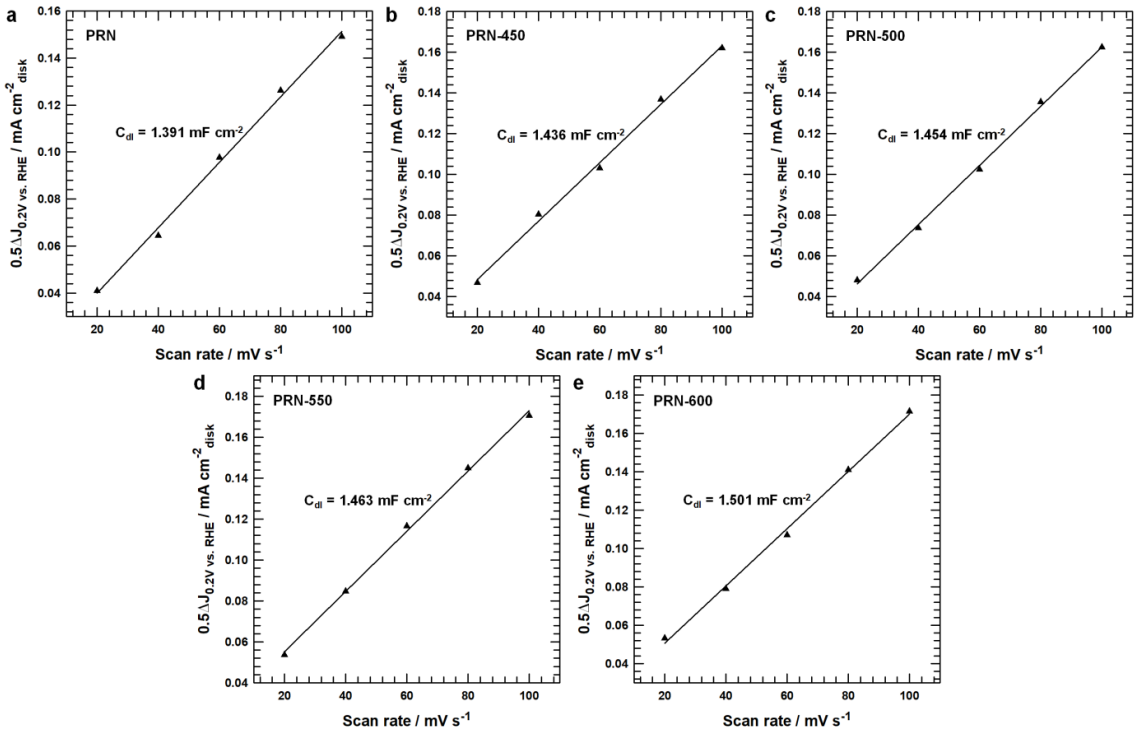

Fig. S12. Linear fitting of the capacitive current as a function of CV scan rate for (a) PRN, (b) PRN-450, (c) PRN-500, (d) PRN-550 and (e) PRN-600.

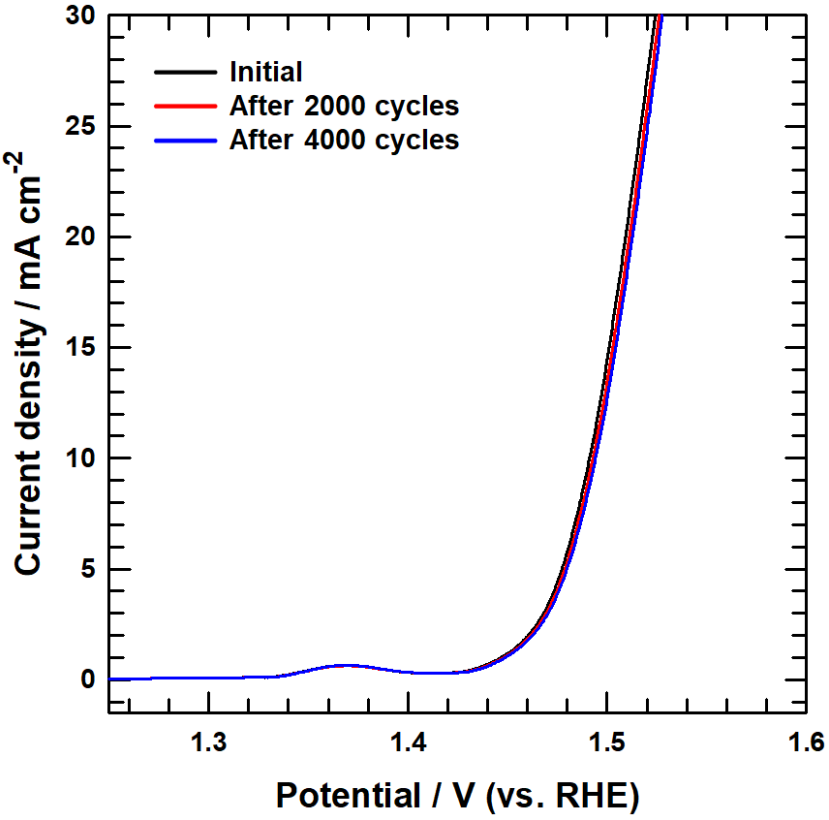

Fig. S13. OER polarization curves of PRN-500 before and after 2000 and 4000 CV cycles. The electrocatalytic durability of PRN-500 was investigated by continuous CV cycles in the potential range of 1.3–1.52 V vs. RHE. The LSV curve of PRN-500 after 4000 CV cycles showed a negligible loss of OER activity, demonstrating the outstanding stability of PRN-500.

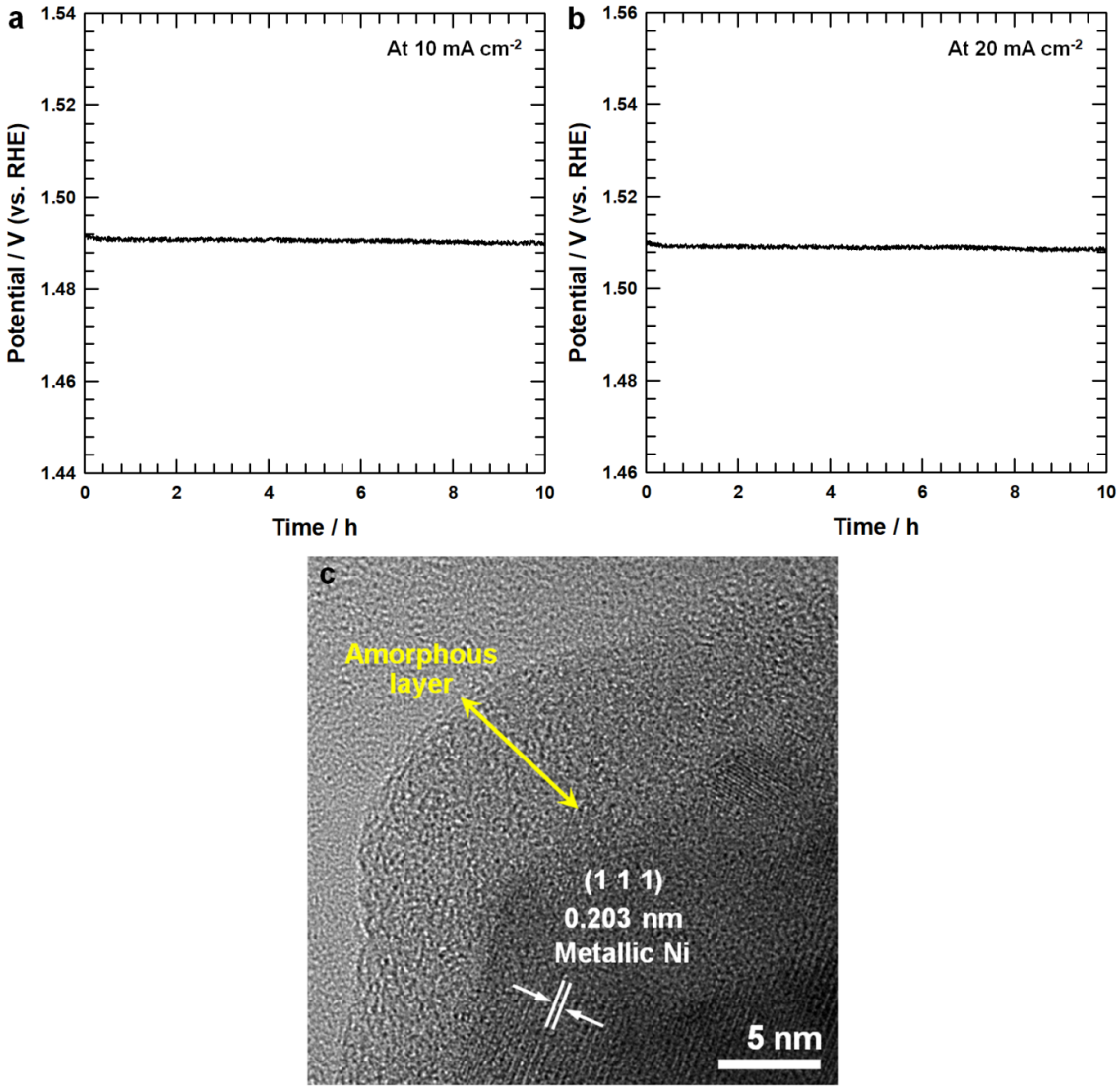

Fig. S14. Chronopotentiometric profiles of PRN-500 recorded over 10 h at a constant current density of (a) 10 mA cm^{-2} and (b) 20 mA cm^{-2}. The long-term stability of PRN-500 was evaluated by chronopotentiometry tests at current densities of 10 and 20 mA cm^{-2}. The initial potentials were maintained well over 10 h, confirming the excellent OER catalytic stability of PRN-500. (c) HR-TEM image of PRN-500 after OER chronopotentiometry test for 10 h. After the chronopotentiometry test, the anchored Ni nanoparticles on pyrochlore oxide surface showed the formation of an amorphous layer. These in-situ formed oxide species under OER conditions serve as the catalytically active sites toward OER. The favorable oxidation nature of Pb and Ru cations in pyrochlore oxide support can facilitate the formation of the amorphous surface layer.

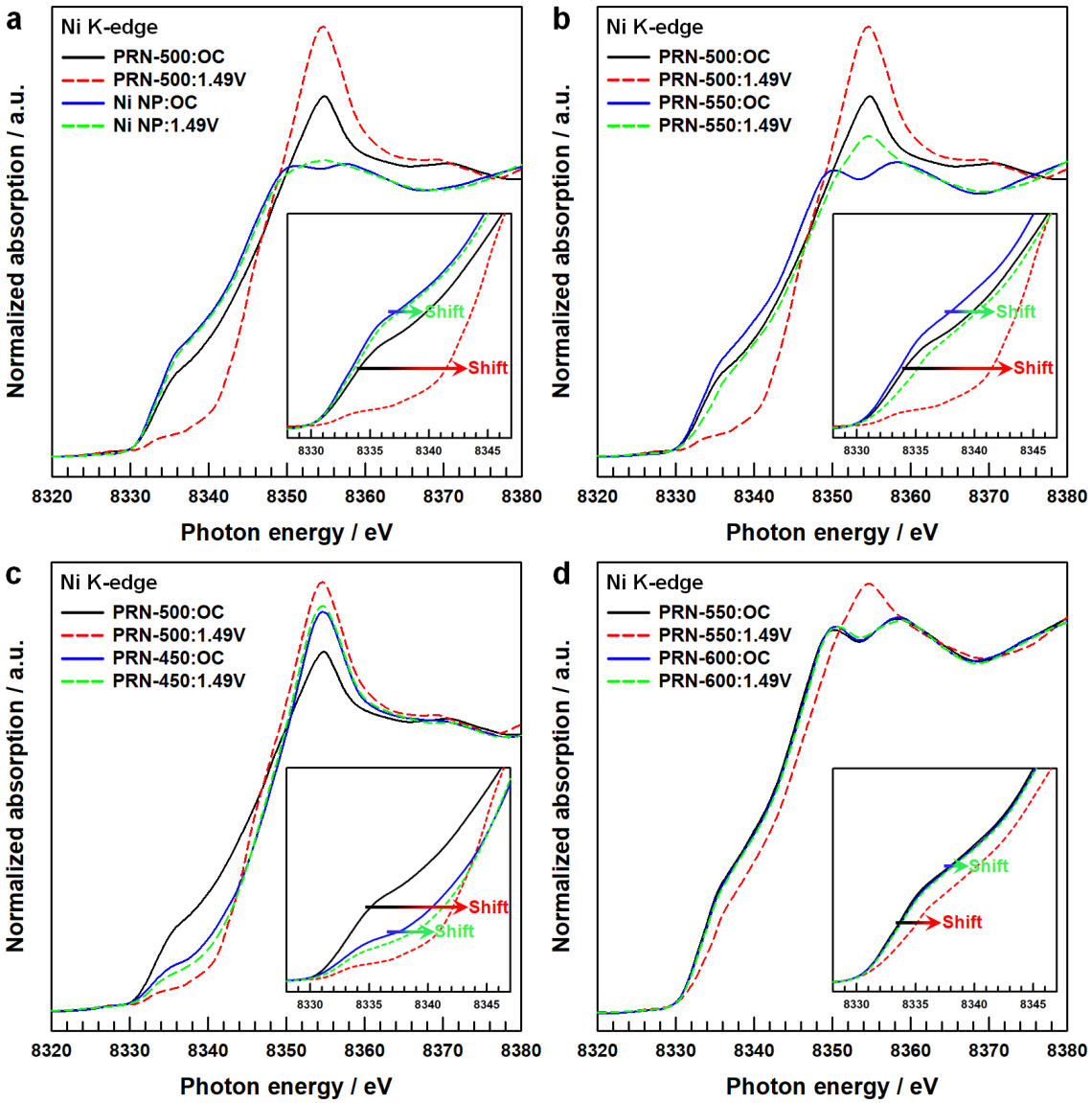

Fig. S15. *Operando* Ni K-edge XANES spectra of (a) PRN-500 and Ni NP, (b) PRN-500 and PRN-550, (c) PRN-450 and PRN-500, (d) PRN-550 and PRN-600 at open circuit potential and at 1.49 V vs. RHE in O_2-saturated 0.1 M KOH electrolyte.

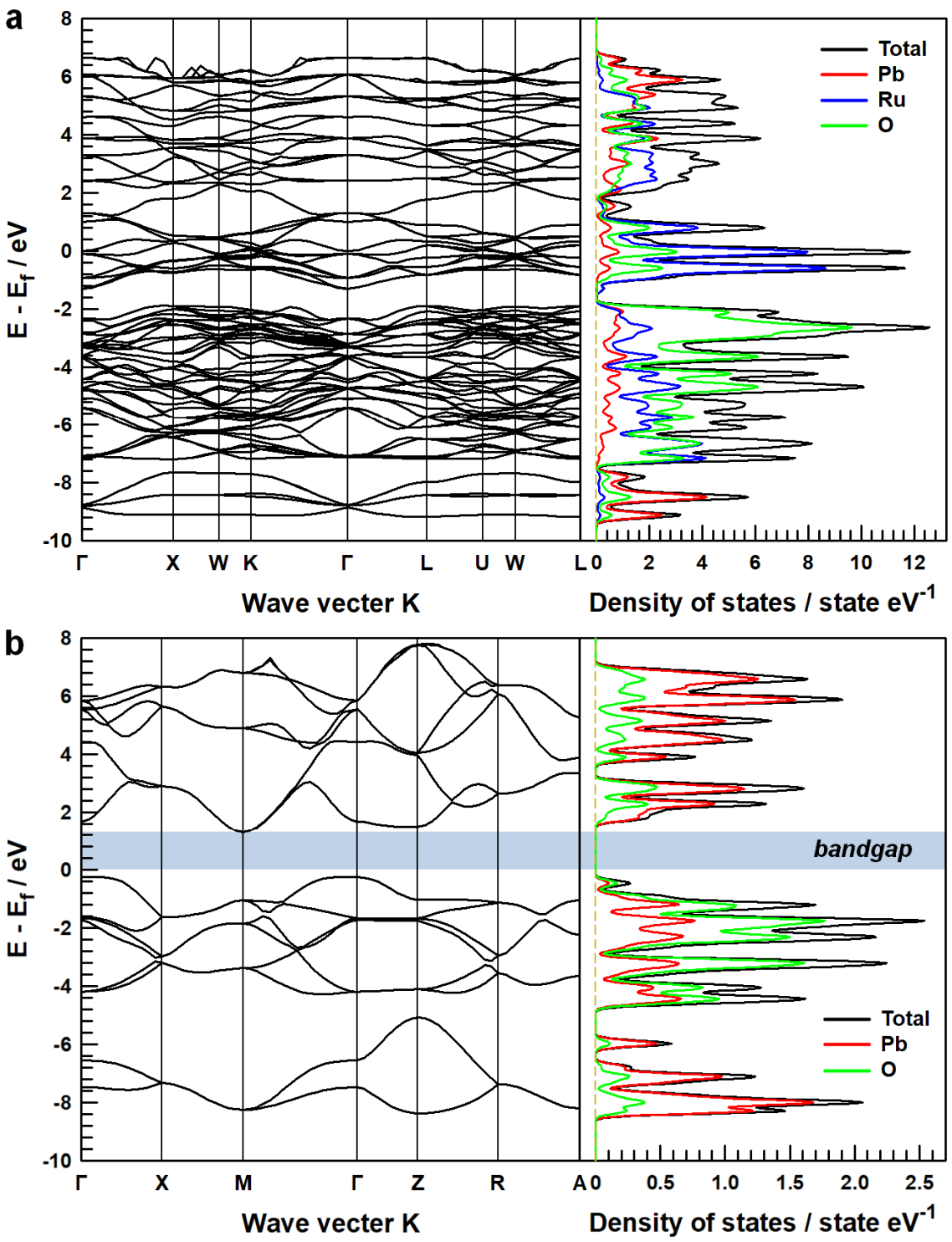

Fig. S16. Electronic band structure and projected density of states for (a) $Pb_2Ru_2O_{6.5}$ and (b) PbO. The Fermi level crosses the bands in $Pb_2Ru_2O_{6.5}$, which suggests $Pb_2Ru_2O_{6.5}$ is metallic. On the other hand, PbO exhibits a band gap.

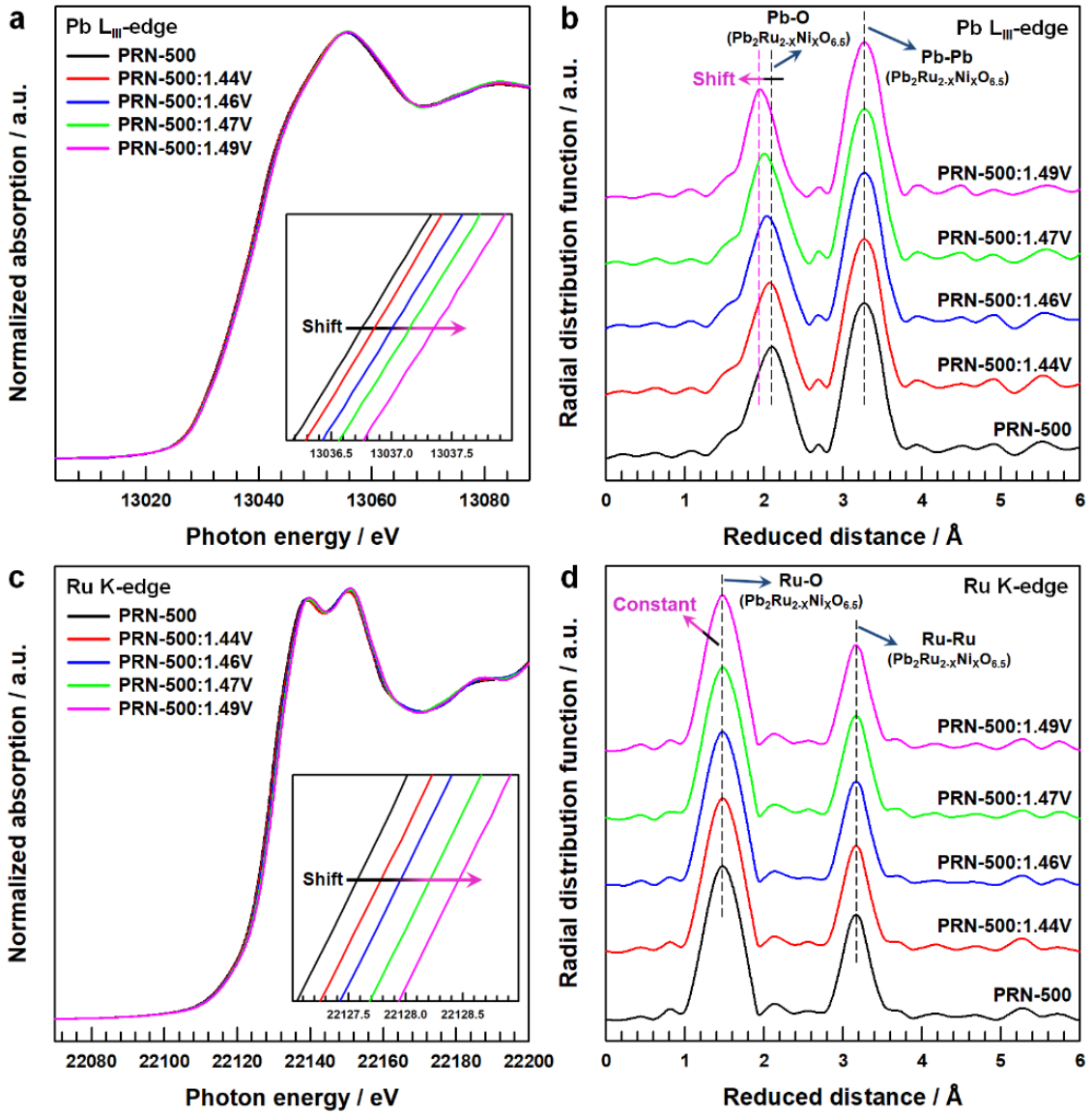

Fig. S17. *Operando* XAS analysis of PRN-500 from 1.44 to 1.49 V vs. RHE in O_2-saturated 0.1 M KOH electrolyte. (a,b) *Operando* Pb L_{III}-edge XANES and EXAFS spectra. (c,d) *Operando* Ru K-edge XANES and EXAFS spectra. Fig. S17a shows the Pb L_{III}-edge XANES spectra of PRN-500 under various potentials. The Pb L_{III}-edge XANES spectrum of PRN-500 showed a positive shift with increasing applied potential, indicating that the A-site Pb cations in the pyrochlore oxide structure were gradually oxidized. Moreover, in the Pb L_{III}-edge EXAFS spectra, the Pb-O bond peak of PRN-500 was gradually shifted toward lower reduced distances as the applied potential increased (Fig. S17b). The oxidation state of the B-site Ru cations in the pyrochlore oxide structure also increased with increasing

applied potential, as shown by the positive shift of the Ru K-edge XANES spectra in Fig. S15c. Therefore, the Pb^{2+} and Ru^{4+} cations in the pyrochlore oxide structure were oxidized to $Pb^{(2+y)+}$ and $Ru^{(4+\delta)+}$during the OER process, which enabled efficient electron transfer from the surface to the inner layers. However, the reduced distance corresponding to the B-site Ru-O bond hardly changed in the Ru K-edge EXAFS spectra, indicating negligible variation in the local geometric structure during the OER process (Fig. S17d). While the local structure of A-site cations and oxygen bonds (Pb-O) in the pyrochlore oxide is rather flexible, the bonds between the B-site cations and oxygen (*i.e.*, Ru-O) form a rigid RuO_6 octahedral structure, leading to a constant reduced distance for Ru-O bonds under OER conditions.[25] Such rigid RuO_6 octahedral structure can contribute to the electrochemical stability of the PRN support during the OER process.

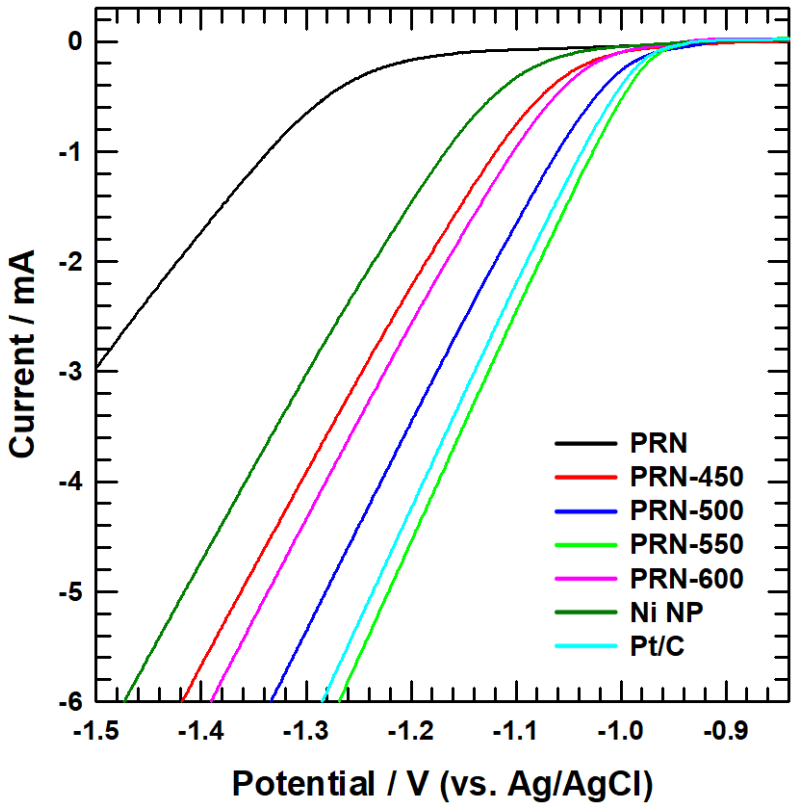

Fig. S18. Pristine HER LSV polarization curves without RHE calibration and *iR* correction for PRN, PRN-X, Ni NP and Pt/C benchmark on a RDE in a N_2-saturated 0.1 M KOH electrolyte.

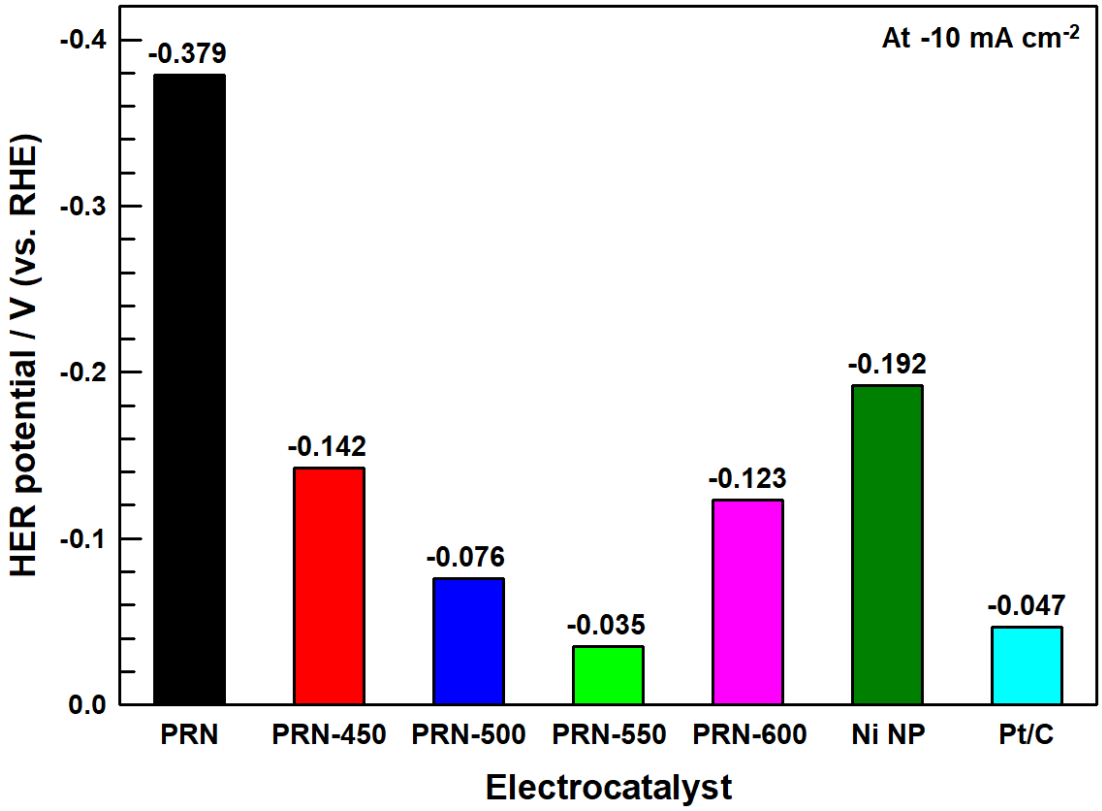

Fig. S19. Comparison of the HER potentials required to achieve a current density of -10 mA cm^{-2} for PRN, PRN-X, Ni NP and Pt/C benchmark.

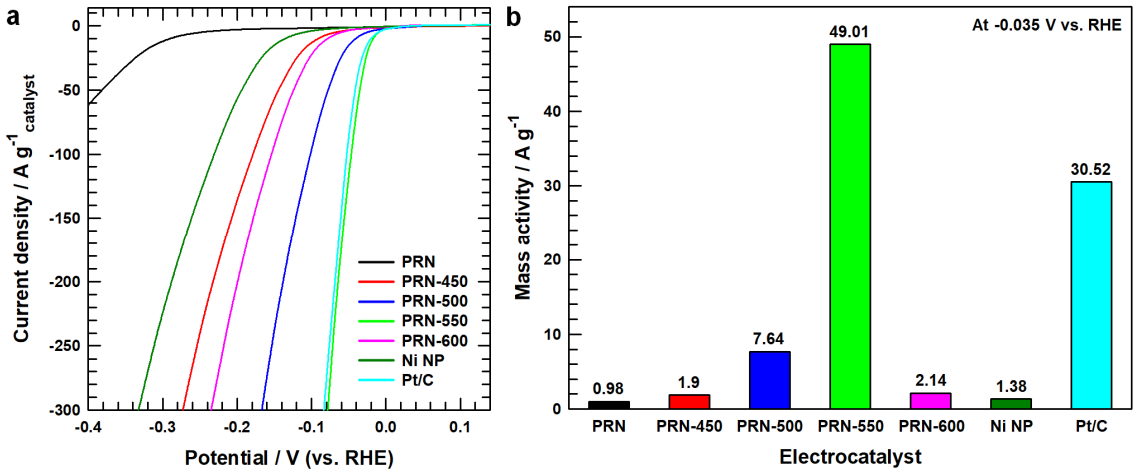

Fig. S20. (a) HER polarization curves normalized to catalyst mass for PRN, PRN-X, Ni NP and Pt/C, measured at a scan rate of 5 mV s^{-1} and 1600 rpm in N_2-saturated 0.1 M KOH electrolyte. (b) Mass activity of PRN, PRN-X, Ni NP and Pt/C benchmark at -0.035 V vs. RHE. The LSV curves normalized by the loading mass of electrocatalyst exhibited a similar trend to that of the LSV curves based on the RDE electrode area. PRN-550 delivered the highest mass activity of 49.01 A g^{-1} at a potential of -0.035 V vs. RHE, which was 50 and 1.6 times higher than that of PRN (0.98 A g^{-1}) and Pt/C (30.52 A g^{-1}), respectively.

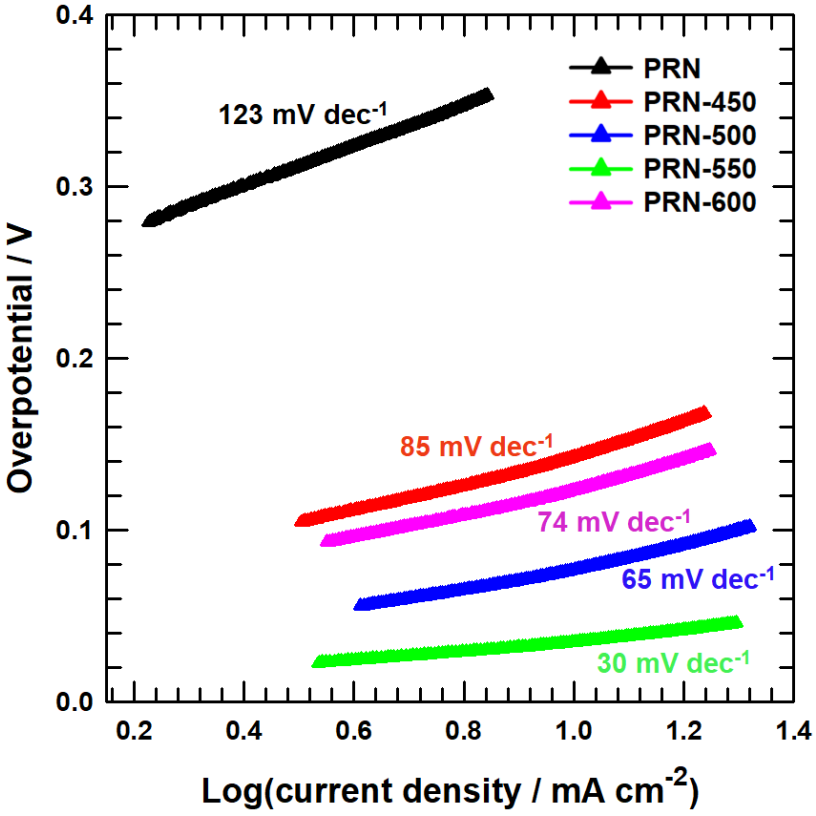

Fig. S21. Tafel plots for PRN and PRN-X at a scan rate of 5 mV s^{-1} and 1600 rpm in N_2-saturated 0.1 M KOH electrolyte.

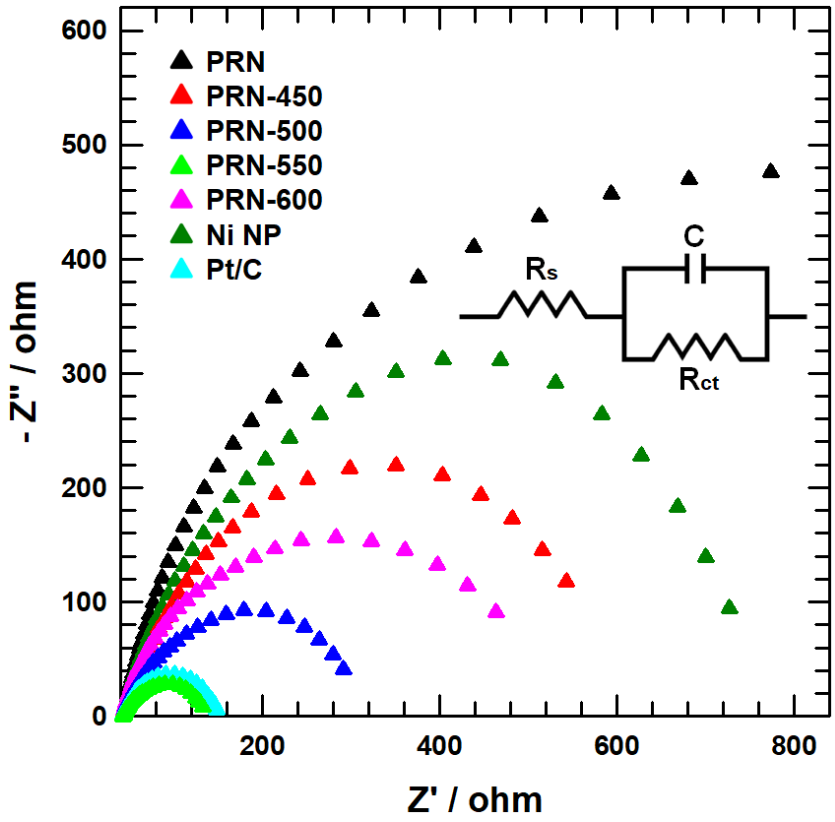

Fig. S22. Nyquist plots for PRN, PRN-X, Ni NP and Pt/C benchmark recorded at -0.035 V vs. RHE in a N_2-saturated 0.1 M KOH electrolyte. The charge transfer resistance (R_{ct}) varied in the order PRN (1415.337 Ω) > Ni NP (684.215 Ω) > PRN-450 (500.154 Ω) > PRN-600 (420.706 Ω) > PRN-500 (248.742 Ω) > Pt/C (105.781 Ω) > PRN-550 (89.421 Ω), further confirming the fast hydrogen evolution kinetics of PRN-550.

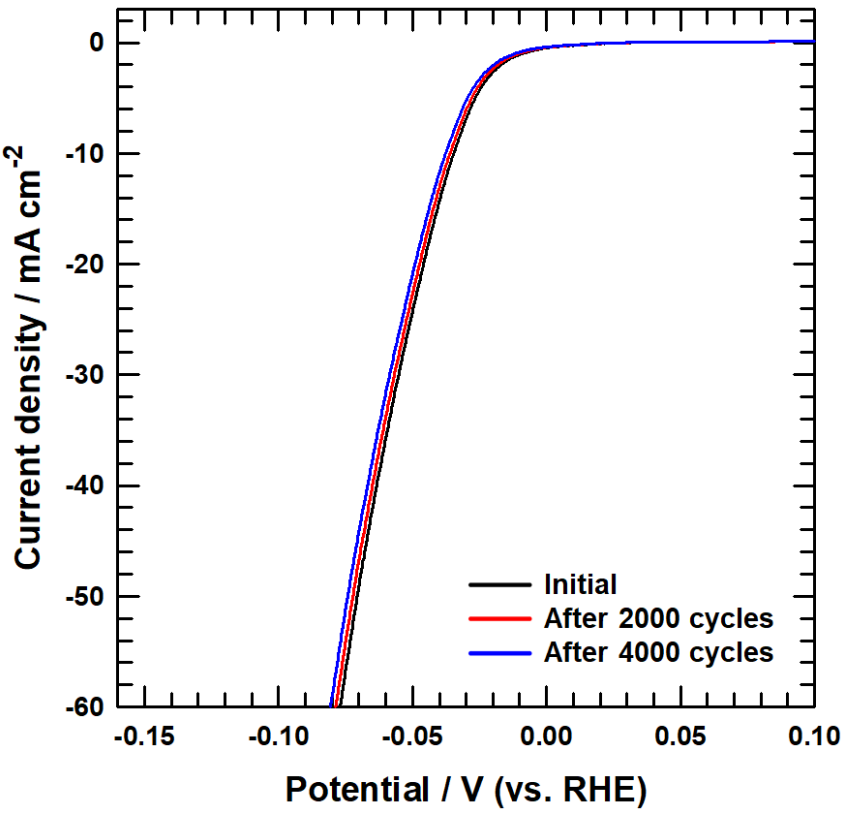

Fig. S23. HER polarization curves of PRN-550 before and after 2000 and 4000 CV cycles. The CV cycles were conducted in the potential range from 0 to -0.1 V vs. RHE to examine the durability of PRN-550. The LSV curve of PRN-550 after 4000 CV cycles showed a negligible loss of HER activity, demonstrating the outstanding durability of PRN-550.

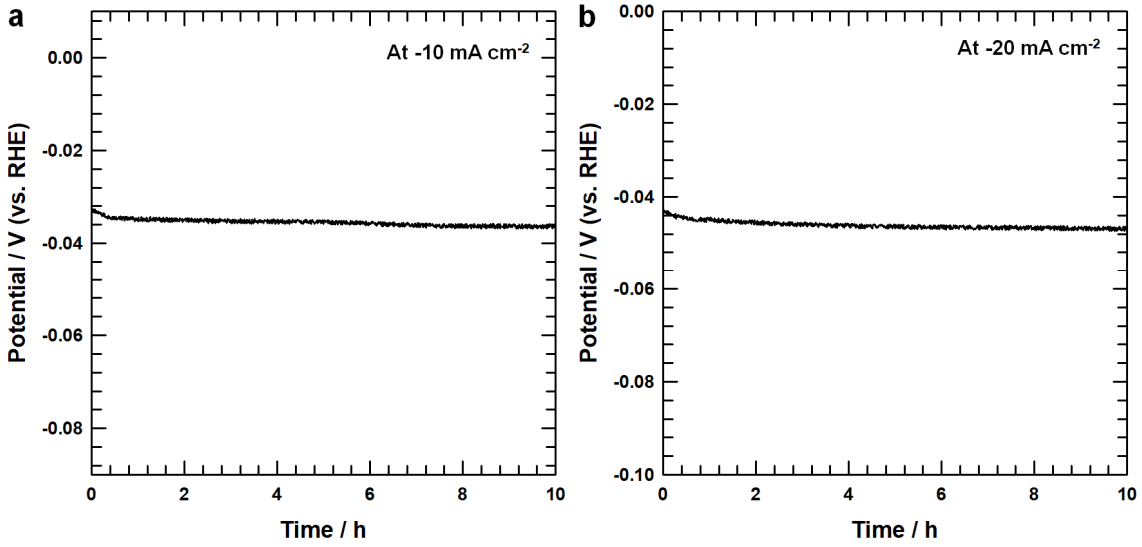

Fig. S24. Chronopotentiometric profiles of PRN-550 recorded over 10 h at a constant current density of (a) 10 mA cm^{-2} and (b) 20 mA cm^{-2}. The long-term stability of PRN-550 was evaluated by chronopotentiometry tests at current densities of -10 and -20 mA cm^{-2}. The initial potentials were maintained well over 10 h, confirming the excellent HER catalytic stability of PRN-550.

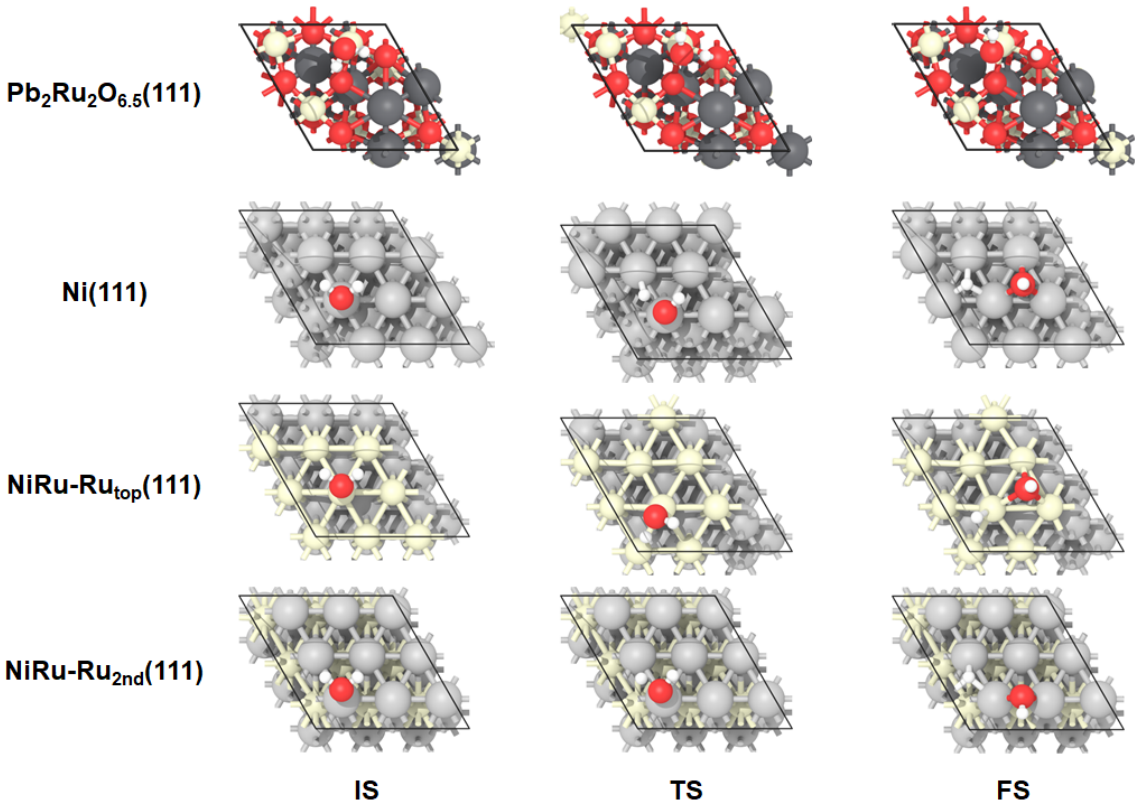

Fig. S25. Atomic configurations of initial state (IS), transition state (TS), and final state (FS) of H_2O dissociation on $Pb_2Ru_2O_{6.5}(111)$, Ni(111), NiRu-$Ru_{top}(111)$ and NiRu-$Ru_{2nd}(111)$ surfaces. Dark grey, ivory, light grey, red and white balls indicate Pb, Ru, Ni, O and H atoms, respectively.

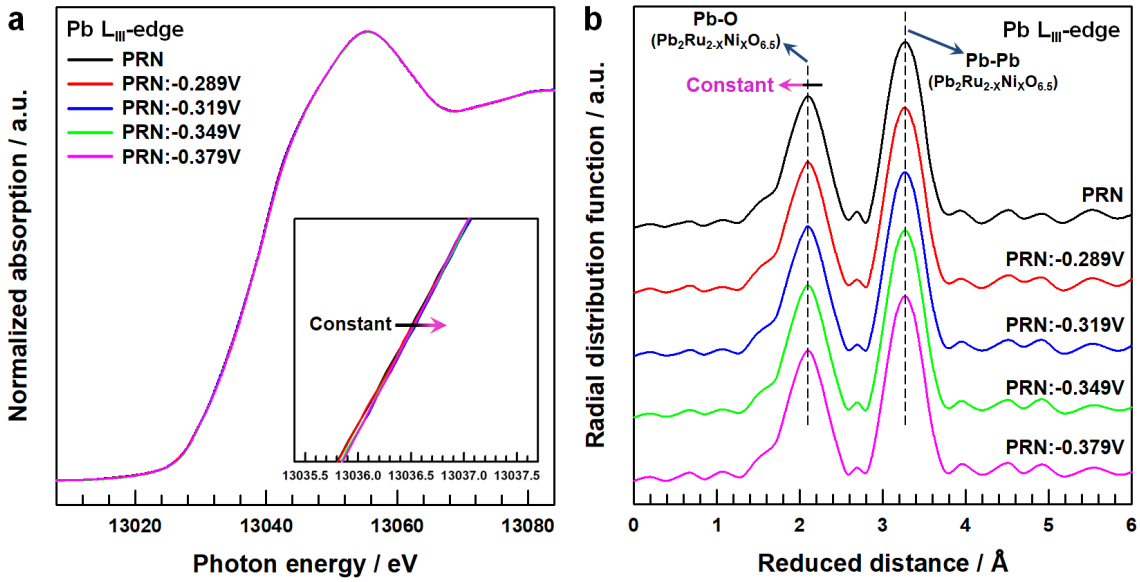

Fig. S26. *Operando* Pb L_{III}-edge (a) XANES and (b) EXAFS spectra of PRN from -0.289 to -0.379 V vs. RHE in a N_2-saturated 0.1 M KOH solution. The potential value of -0.379 V vs. RHE indicates the HER potential of PRN to achieve a current density of -10 mA cm^{-2}. There were no obvious changes in both XANES and EXAFS spectra with decreasing HER potential, indicating the constant oxidation states of Pb cations and local structure of Pb-O bond.

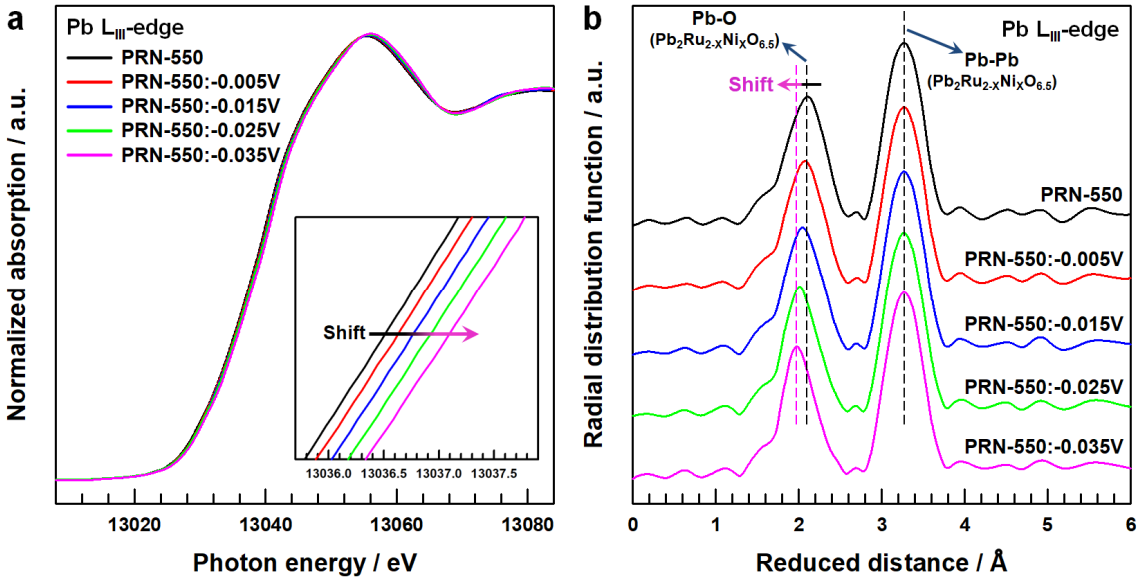

Fig. S27. *Operando* Pb L_{III}-edge (a) XANES and (b) EXAFS spectra of PRN-550 from -0.005 to -0.035 V vs. RHE in a N_2-saturated 0.1 M KOH solution. The potential value of -0.035 V vs. RHE indicates the HER potential of PRN-550 to achieve a current density of -10 mA cm^{-2}. PRN-550 shows the positively shifted Pb L_{III}-edge XANES spectra and negatively shifted reduced distance of Pb-O bonds in Pb L_{III}-edge EXAFS spectra with decreasing applied potential. These results imply that the Pb cations at A-site pyrochlore oxide structure in PRN-550 are gradually oxidized when the HER occurred.

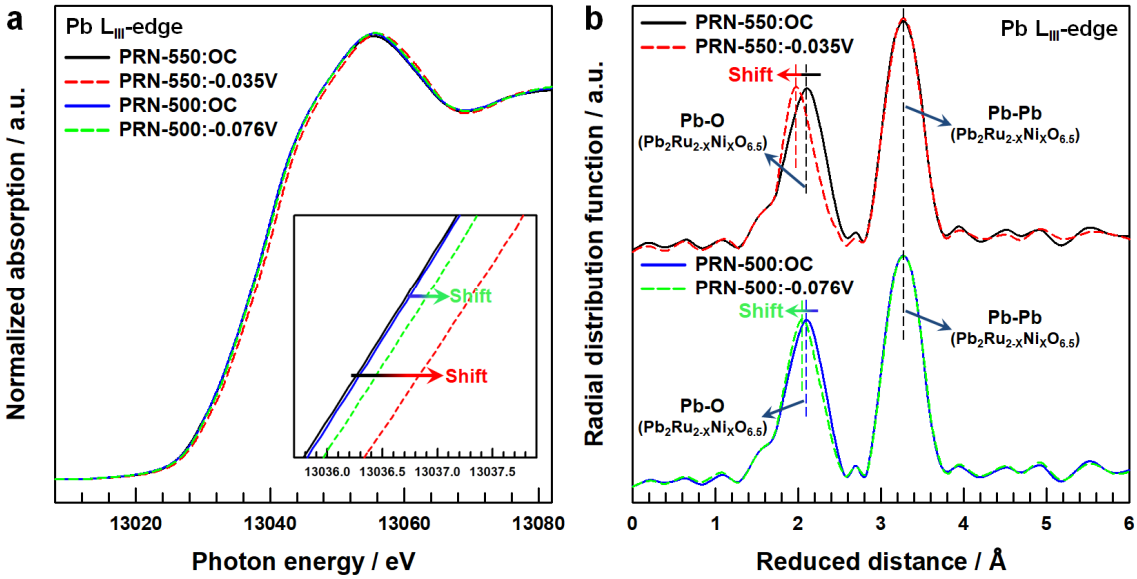

Fig. S28. *Operando* Pb L_{III}-edge (a) XANES and (b) EXAFS spectra of PRN-500 and PRN-550 at open circuit potential and the HER potential at a current density of -10 mA cm^{-2} for PRN-500 (-0.076 V vs. RHE) and PRN-550 (-0.035 V vs. RHE) in a N_2-saturated 0.1 M KOH electrolyte.

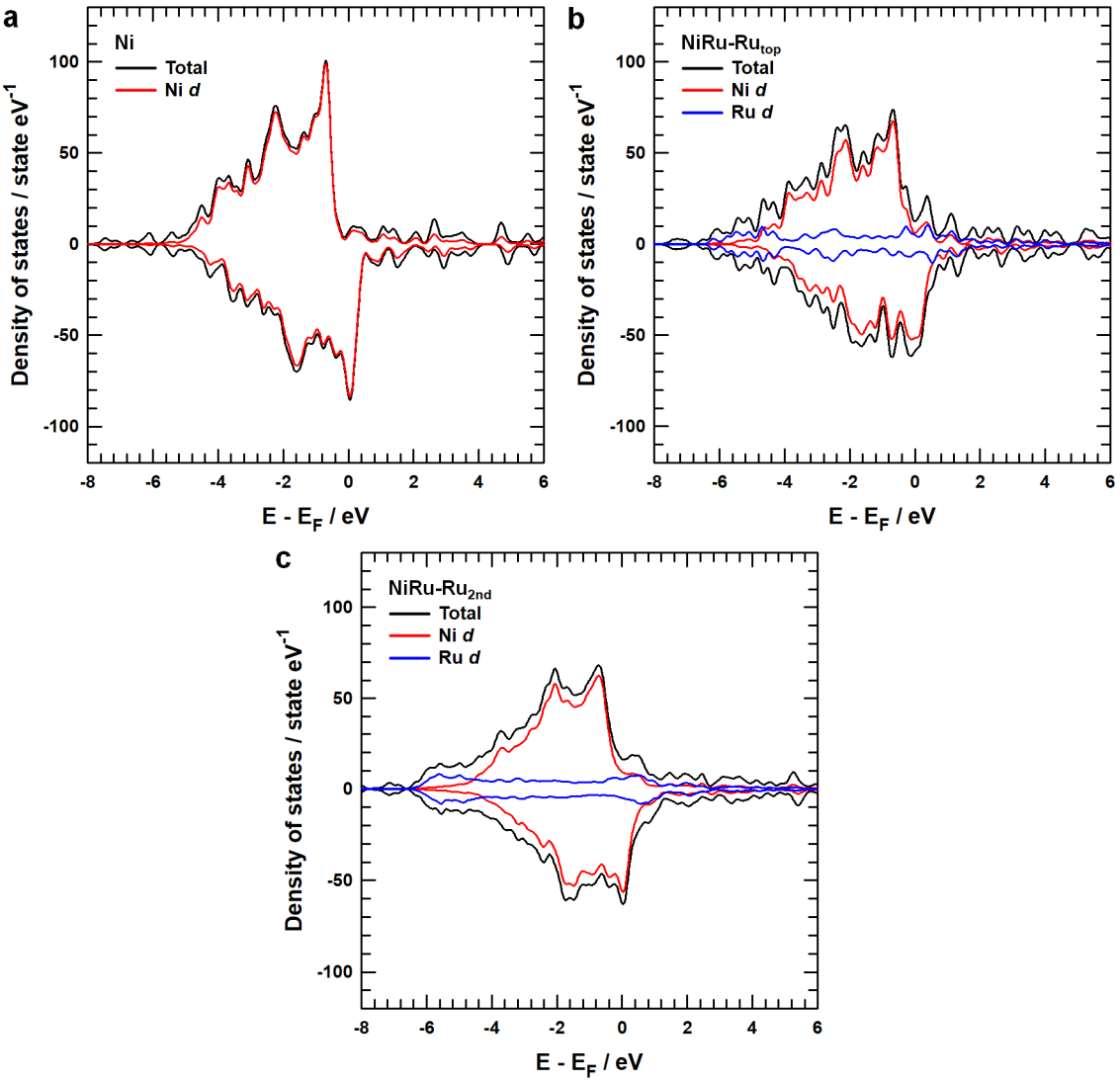

Fig. S29. Projected density of states for (a) Ni, (b) NiRu-Ru_{top}, and (c) NiRu-Ru_{2nd}, respectively. The black line indicates the total density of states, while red and blue lines are the projected density of states of Ni *d* and Ru *d*, respectively.

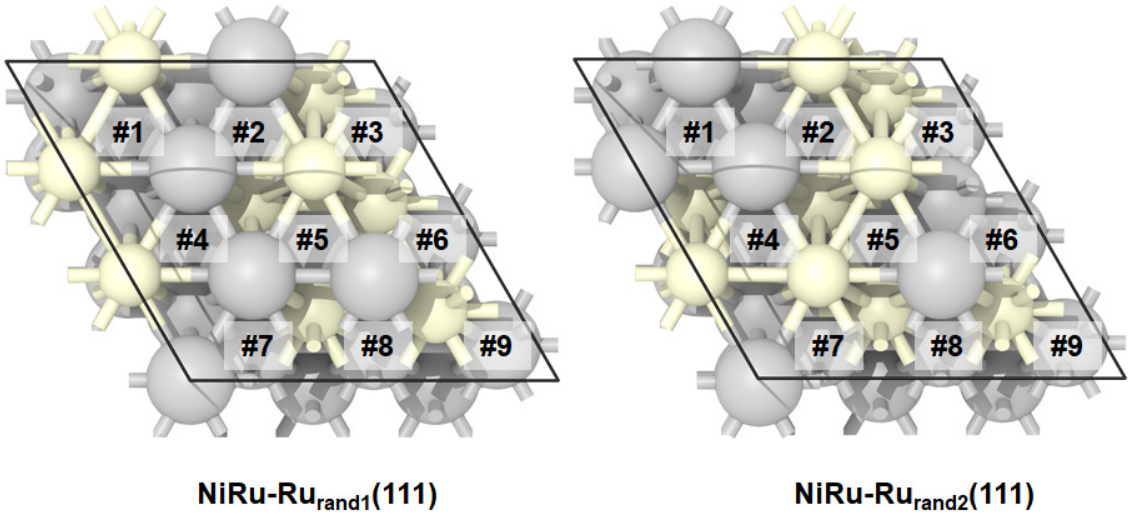

Fig. S30. Atomic configurations of NiRu-Ru$_{rand1}$(111) and NiRu-Ru$_{rand2}$(111). Light grey and ivory balls indicate Ni and Ru atoms, respectively.

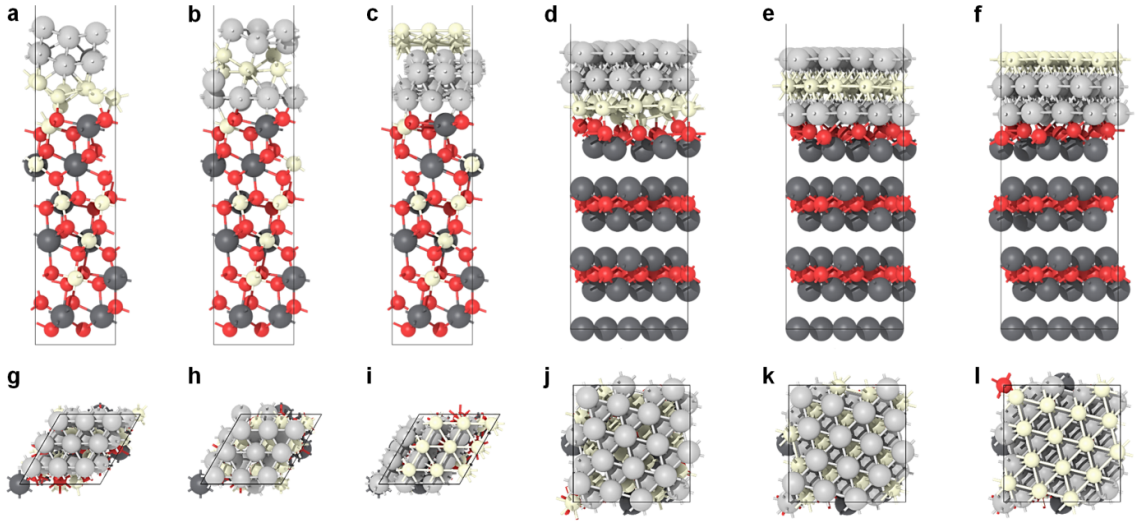

Fig. S31. Geometry optimized structures of (a,g) NiRu-Ru_{btm}/$Pb_2Ru_2O_{6.5}$, (b,h) NiRu-Ru_{mid}/$Pb_2Ru_2O_{6.5}$, (c,i) NiRu-Ru_{top}/$Pb_2Ru_2O_{6.5}$, (d,j) NiRu-Ru_{btm}/PbO, (e,k) NiRu-Ru_{mid}/PbO, and (f,l) NiRu-Ru_{top}/PbO. (top row) side-view and (bottom row) top-view. Dark grey, ivory, red and light grey balls indicate Pb, Ru, O and Ni atoms, respectively.

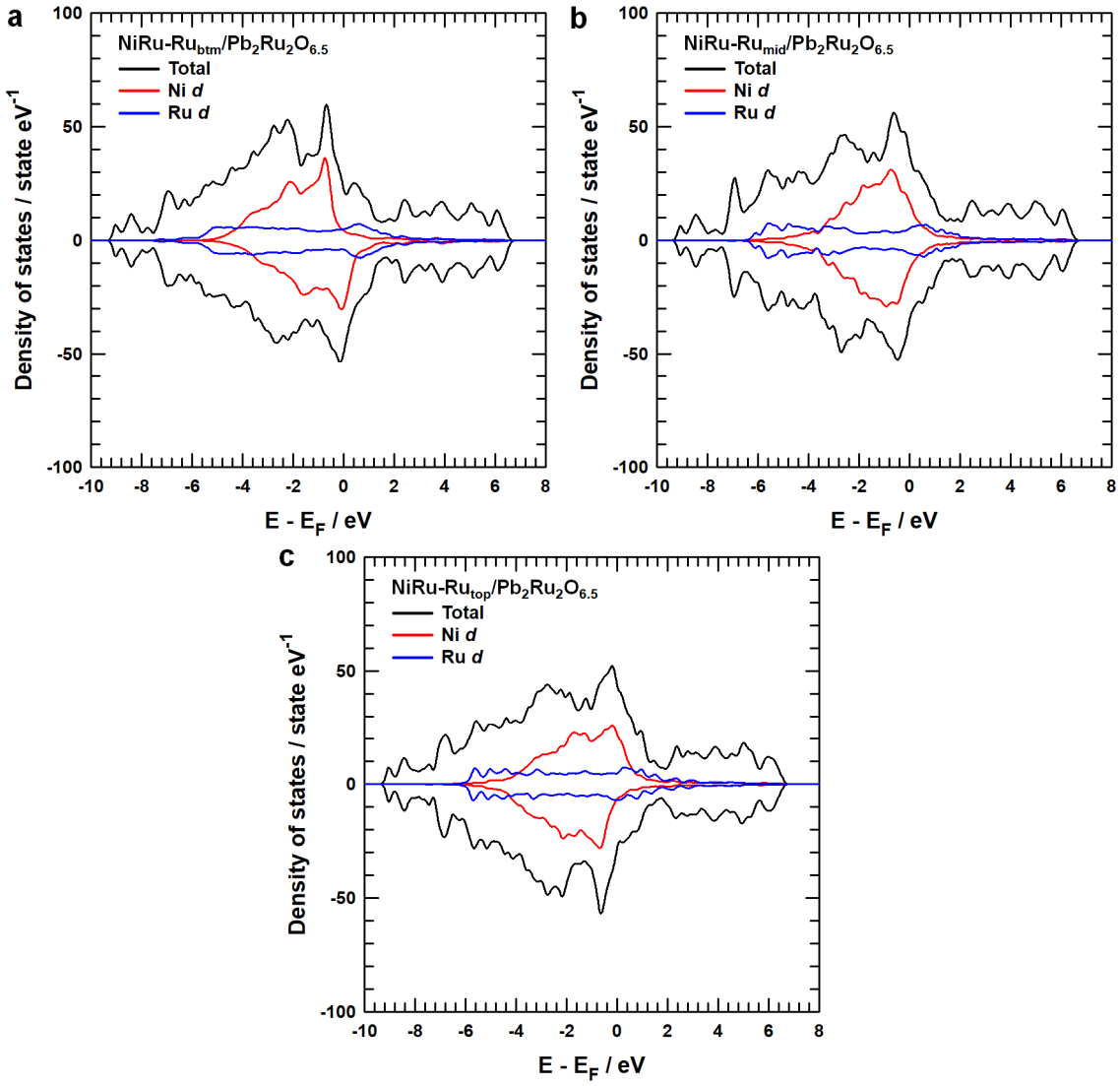

Fig. S32. Projected density of states for NiRu/$Pb_2Ru_2O_{6.5}$. At the NiRu alloy structure, a layer of Ru is located at (a) bottom (NiRu-Ru_{btm}/$Pb_2Ru_2O_{6.5}$), (b) middle (NiRu-Ru_{mid}/$Pb_2Ru_2O_{6.5}$), and (c) top (NiRu-Ru_{top}/$Pb_2Ru_2O_{6.5}$). The black line indicates the total density of states, while red and blue lines are the projected density of states of Ni *d* and Ru *d*, respectively.

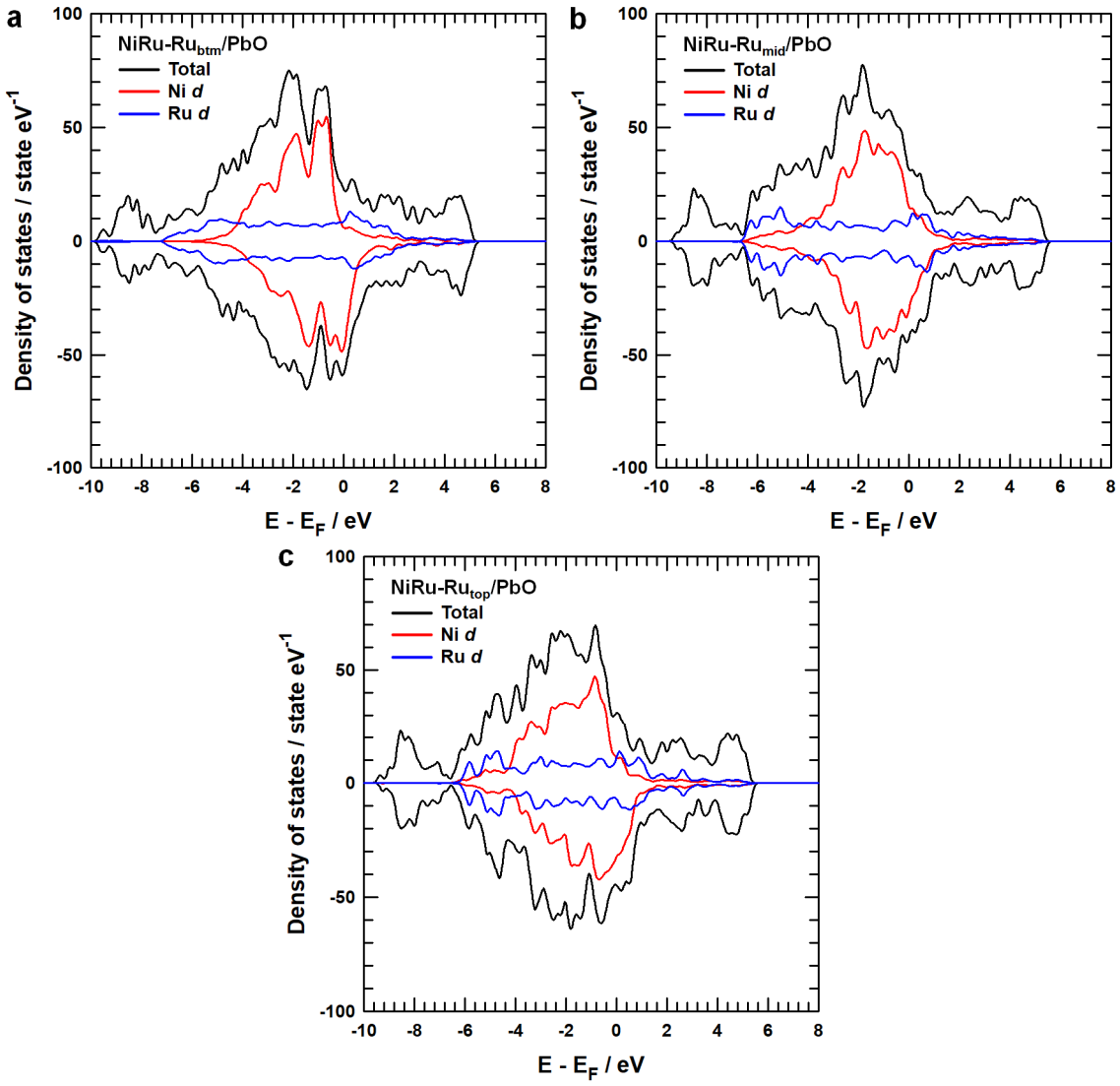

Fig. S33. Projected density of states for NiRu/PbO. At the NiRu alloy structure, a layer of Ru is located at (a) bottom (NiRu-Ru$_{btm}$/PbO), (b) middle (NiRu-Ru$_{mid}$/PbO), and (c) top (NiRu-Ru$_{top}$/PbO). The black line indicates the total density of states, while red and blue lines are the projected density of states of Ni *d* and Ru *d*, respectively.

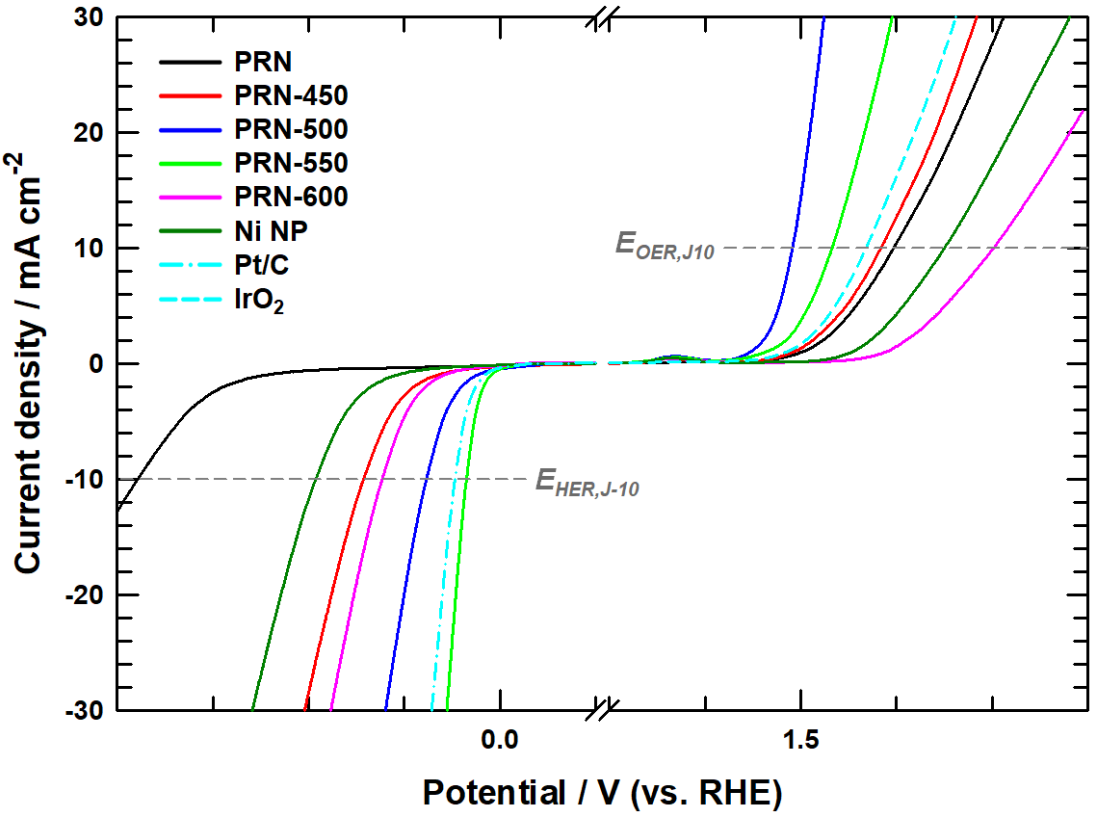

Fig. S34. *iR*-corrected OER and HER polarization curves of PRN, PRN-X, Ni NP, IrO_2 and Pt/C at a scan rate of 5 mV s^{-1} and 1600 rpm in 0.1 M KOH electrolyte. To further investigate the bifunctionality of the adopted electrocatalysts, the OER and HER bifunctional catalytic activity was calculated by subtracting the HER potential at a current density of -10 mA cm^{-2} from OER potential at a current density of 10 mA cm^{-2} ($\Delta E = E_{OER,J10} - E_{HER,J-10}$).

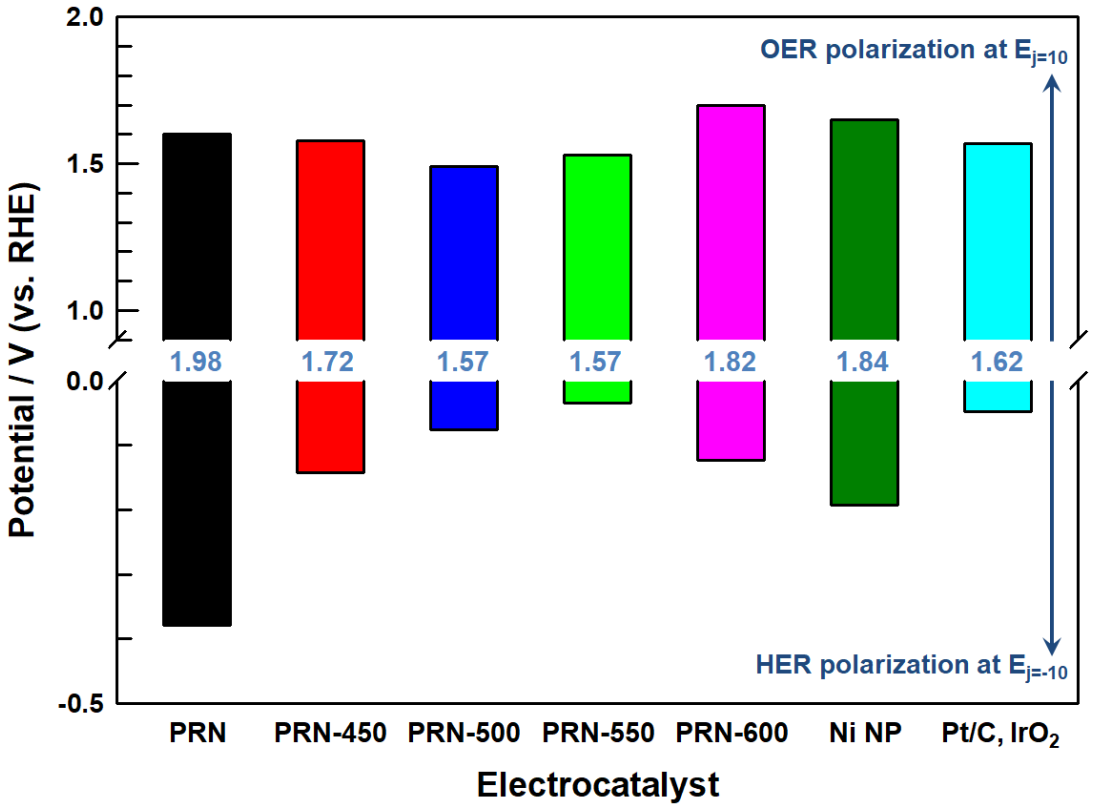

Fig. S35. The differences in the potentials (ΔE) required to achieve OER and HER current densities of 10 mA cm^{-2}. The results suggest that the PRN-550 exhibits the superior HER catalytic activity, while the PRN-500 shows the best OER catalytic activity. Inspired by their outstanding performance (ΔE value of 1.53 V), a two-electrode electrolyzer was assembled using PRN-500 as the anodic catalyst and PRN-550 as the cathodic catalyst (PRN-550 || PRN-500) for overall water splitting. For comparison, the reference anodic catalyst (IrO_2) and the reference cathodic catalyst (Pt/C) were also employed to construct a two-electrode electrolyzer (Pt/C || IrO_2).

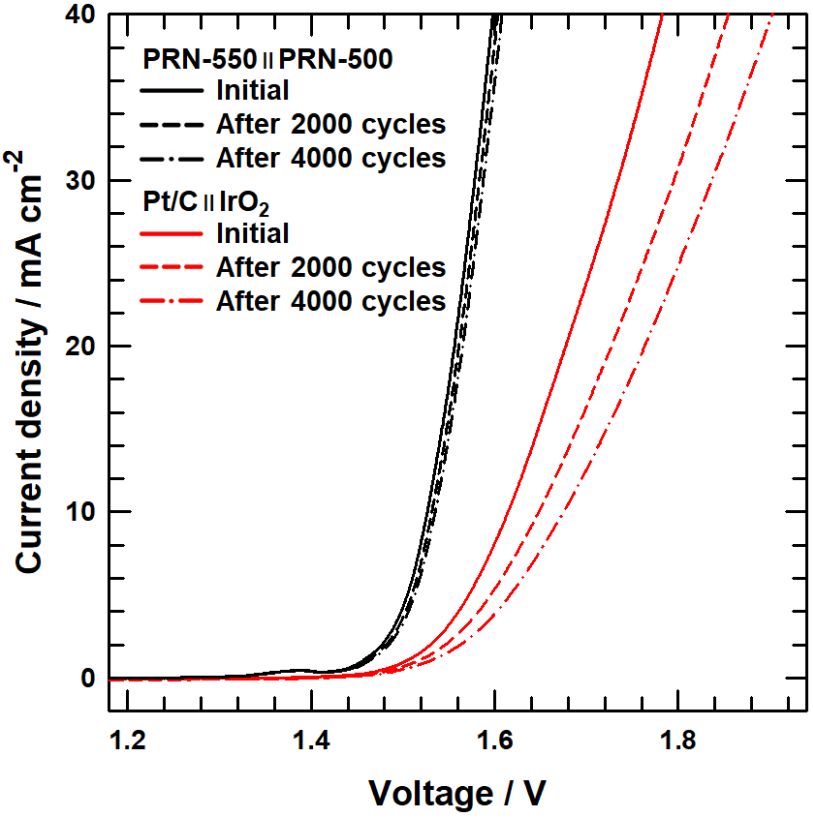

Fig. S36. Polarization curves of PRN-550 || PRN-500 and Pt/C || IrO_2 cell before and after 2000 and 4000 CV cycles in 0.1 M KOH electrolyte. The 4000 cycle continuous CV measurements were conducted in the voltage range from 1.3 to 1.7 V to examine the durability of as-fabricated electrolyzers. The excellent durability of PRN-550 || PRN-500 cell was observed by confirming that the LSV curves after 2000 and 4000 cycles nearly overlap with the initial LSV curve. However, Pt/C || IrO_2 cell showed positively shifted LSV curves after 2000 and 4000 CV cycles, representing the poor cycling durability.

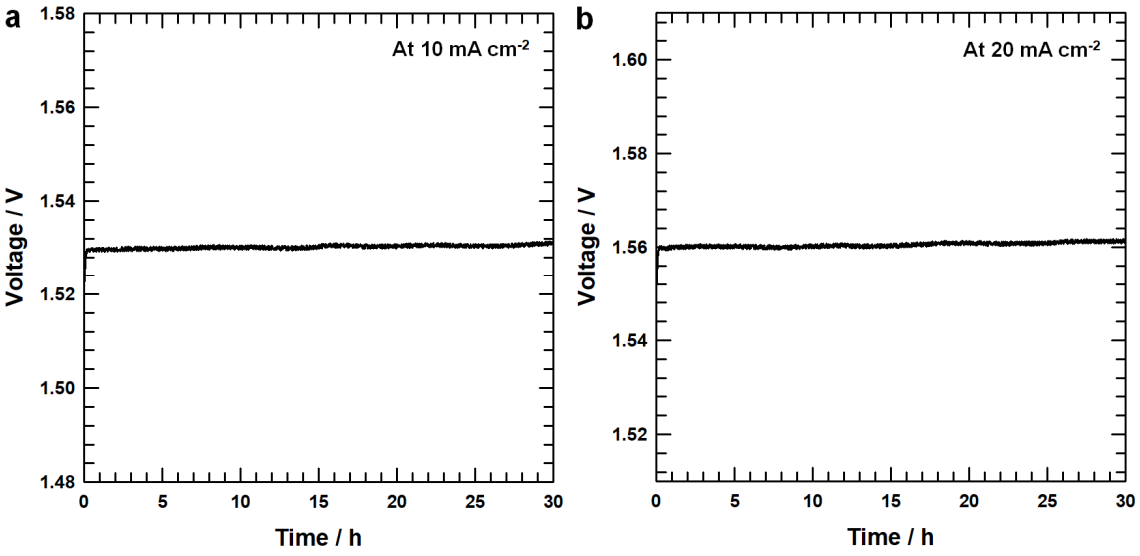

Fig. S37. Chronopotentiometric profiles of PRN-550 || PRN-500 cell recorded over 30 h at a constant current density of (a) 10 mA cm^{-2} and (b) 20 mA cm^{-2} in 0.1 M KOH electrolyte. The potentials responses during 30 h at current densities of 10 and 20 mA cm^{-2} showed negligible changes, demonstrating outstanding water splitting stability.

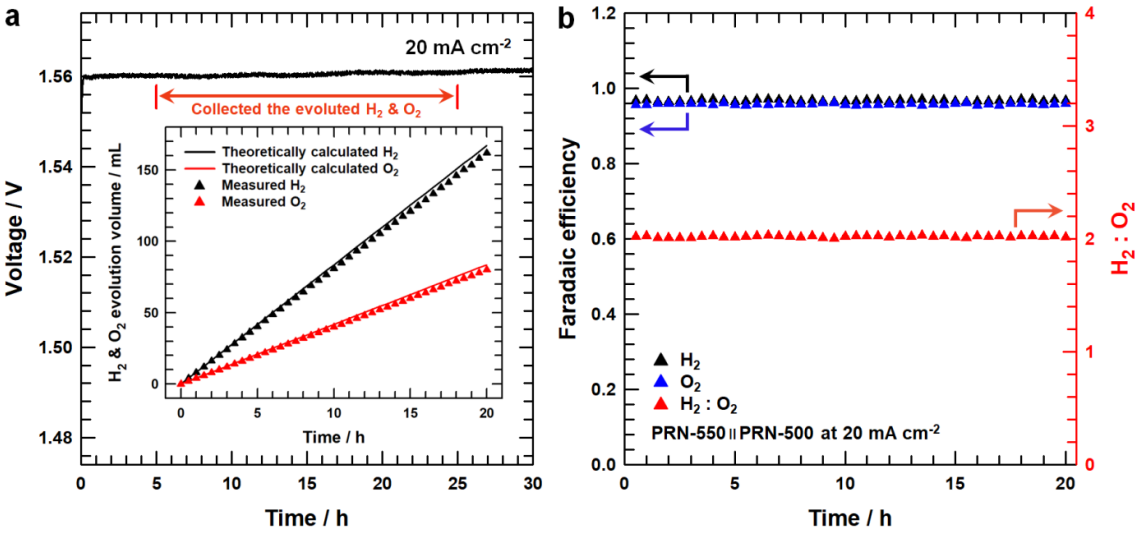

Fig. S38. (a) Theoretical and experimental H_2 and O_2 gas evolution volume of PRN-550 || PRN-500 cell for 20 h during chronopotentiometry measurement at a constant current density of 20 mA cm^{-2}. (b) Gas ratio and Faradaic efficiency of evolved H_2 and O_2 gas from the PRN-550 || PRN-500 cell for 20 h during chronopotentiometry measurement at a constant current density of 20 mA cm^{-2}.

Table S1. OER activity of PRN-500 compared to other reported state-of-the art electrocatalysts.

OER electrocatalysts	Electrolyte	Overpotential (mV) (at j = 10 mA cm^{-2})	Ref
$NiFe_X$@NiCu	1.0 M KOH	316	26
CoO_X NPs/BNG	0.1 M KOH	300	27
$Co(S_XSe_{1-X})_2$	1.0 M KOH	280	28
Pt-CoS_2/CC	1.0 M KOH	300	29
$Pb_2Ru_2O_{6.5}$	0.1 M KOH	418	17
P-$Tl_2Ru_2O_7$	0.1 M KOH	274	18
P-$Bi_2Rh_2O_{6.8}$	0.1 M KOH	290	30
$Bi_2Ru_2O_7$	0.1 M KOH	448	31
Ni-Fe LDH	0.1 M KOH	308	32
Co-Fe-O/rGO	1.0 M KOH	340	33
$Ni_{1-y-z}Fe_yCr_zO_x$	1.0 M KOH	320	34
Ni-Fe@rGO	1.0 M KOH	350	35
CoMn-LDH/CNT	1.0 M KOH	335	36
H-Pt/$CaMnO_3$	0.1M KOH	590	37
$Ni_XCo_{3-X}O_4$	1.0 M KOH	370	38
$Ni_{0.33}Co_{0.67}S_2$	1.0 M KOH	330	39
Co_3S_4 HNSs	1.0 M KOH	307	40
$Ni(OH)_2$	0.1M KOH	331	41
FeP_X/Fe-N-C/NPC	1.0 M KOH	325	42
Co_4N/CNW/CC	1.0 M KOH	310	43
PRN-500	**0.1 M KOH**	**260**	**This work**

Table S2. The XPS O 1s peak position and the relative atomic percentages of various oxygen species in PRN and PRN-X.

	Fitting of the O 1s peak binding energy [eV] (Relative atomic percentage [%])			
	O_L	O_V	O_{surf}	O_{adv}
PRN	529.3 (69.13)	530.96 (16.14)	531.97 (11.28)	533.37 (3.45)
PRN-450	529.32 (65.56)	530.95 (20.12)	531.98 (11.06)	533.38 (3.26)
PRN-500	529.31 (62.34)	530.97 (23.53)	531.96 (11.09)	533.38 (3.04)
PRN-550	529.29 (59.75)	530.96 (25.94)	531.97 (11.29)	533.38 (3.02)
PRN-600	528.84 (86.25)	-	531.99 (11.12)	533.4 (2.63)

O 1s spectra can be deconvoluted into four different characteristic peaks, i.e., lattice oxygen species (O_L, ~529.3 eV for $Pb_2Ru_{2-X}Ni_XO_{6.5}$ or $Pb_2Ru_{2-X}O_{6.5}$ pyrochlore oxide (Fig. 3a) and ~528.85 eV for tetragonal PbO (α-PbO)), oxygen lattice sites located in the vicinity of oxygen vacancies (O_V, ~530.96 eV for $Pb_2Ru_{2-X}Ni_XO_{6.5}$ or $Pb_2Ru_{2-X}O_{6.5}$ pyrochlore oxide (Fig. 3a)), surface oxygen species including hydroxyl group (-OH), O^{2-}, O_2^{2-}, O^-, OH^- (O_{surf}, ~531.98 eV) and adventitious species (O_{adv}, ~533.4 eV).[44-46]

Table S3. HER activity of PRN-550 compared to other reported state-of-the art electrocatalysts.

HER electrocatalysts	Electrolyte	Overpotential (mV) (at j = -10 mA cm^{-2})	Ref.
Pt-CoS_2/CC	1 M KOH	24	29
NiCoP/CC	1 M KOH	62	47
Co_XMn_YCH/NF	1 M KOH	180	48
Ni_5P_4 Film	1 M KOH	150	49
MoC_X	1 M KOH	151	50
Bulk Mo_2C	1 M KOH	195	51
NiRu-N doped carbon	1 M KOH	32	19
NiFe-LDH-NS@DG	1 M KOH	115	52
Fe-CoP/Ti	1 M KOH	128	53
$NiFeO_X$@NiCu	1 M KOH	66	26
CoRu-N doped carbon	1 M KOH	45	54
Zn-Co-S NN/CFP	1 M KOH	234	55
CoP/CC	1 M KOH	209	56
CoRu-N doped graphene	1 M KOH	28	57
Pt-$(OH)_2$/CC	1 M KOH	32	58
NiFe LDHs	1 M KOH	219	59
Porous $NiSe_2$ nanosheet	1 M KOH	184	60
Cu@NiFe LDH	1 M KOH	116	61
Pt-Ni_3N/Ni	1 M KOH	40	62
Ni_2P	1 M KOH	220	63
PRN-550	**0.1 M KOH**	**35**	**This work**

Table S4. Activation barrier energies and transition state geometries for H_2O dissociation on various surfaces.

Model	E_a^{cor} (eV)	E_a^{uncor} (eV)	d_{O-H} (Å)	d_{S-O} (Å)	d_{S-H} (Å)	θ_{H-O-H}
$Pb_2Ru_2O_{6.5}$(111)	0.12	0.24	1.282	2.136	1.188	108.6
Ni(111)	0.77	0.98	1.565	1.928	1.696	103.1
	(0.89[64], 0.71[65], 0.90[66], 0.92[67], 0.795[68], 0.69[69])		(1.55[65], 1.586[66], 1.48[68], 1.538[69])	(1.88[68], 1.937[69])	(1.14[68], 1.764[69])	(103.8[66], 120.0[68], 104.7[69])
NiRu-Ru_{top}(111)	0.57	0.75	1.316	2.011	1.933	107.0
NiRu-Ru_{2nd}(111)	0.69	0.89	1.509	1.917	1.676	101.9

Table S5. Calculated the Gibbs free energies of the H adsorption on different sites.

Model	ΔG_{H^*} (eV)								
	#1	#2	#3	#4	#5	#6	#7	#8	#9
NiRu-Ru_{rand1}(111)	-0.15	-0.26	-0.24	-0.16	-0.17	-0.21	-0.28	-0.31	-0.22
NiRu-Ru_{rand2}(111)	-0.29	-0.28	-0.28	-0.13	-0.33	-0.27	-0.25	-0.18	-0.23
Ni(111)	-0.32								
NiRu-Ru_{top}(111)	-0.14								
NiRu-Ru_{2nd}(111)	0.12								

Table S6. Water splitting activity of PRN-550 || PRN-500 system compared to other reported state-of-the art electrocatalysts.

Catalysts	Support	Electrolyte	Overpotential (mV) (at j = 10 mA cm^{-2})	Ref.
NiFe-LDH@NiCu || $NiFeO_X$@NiCu	N/A	1 M KOH	290	26
$Co(S_{0.71}Se_{0.29})_2$ || $Co(S_{0.22}Se_{0.78})_2$	Carbon	1 M KOH	400	28
Pt-CoS_2/CC || Pt-CoS_2/CC	Carbon cloth	1 M KOH	320	29
$NiCo_2O_4$ || $Ni_{0.33}Co_{0.67}S_2$	Ti foil	1 M KOH	490	39
CoS_2 HNSs || CoS_2 HNSs	Carbon paper	1 M KOH	450	40
FeP_x/Fe–N–C/NPC || FeP_x/Fe–N–C/NPC	N-, P-codoped carbon (NPC)	1 M KOH	350	42
Ni_5P_4 || Ni_5P_4	N/A	1 M KOH	470	49
Zn−Co−S NN/CFP || Zn−Co−S NN/CFP	Carbon paper	1 M KOH	480	55
β-$Ni(OH)_2$ || $NiSe_2$	Carbon paper	1 M KOH	540	60
Cu@NiFe LDH || Cu@NiFe LDH	N/A	1 M KOH	310	61
Ni_2P || Ni_2P	Ni foam	1 M KOH	400	63
Co−P || Co−P	N/A	1 M KOH	400	70
NiCoFe LTHs || NiCoFe LTHs	Carbon fiber cloth (CFC)	1 M KOH	320	71
NiSe || Ni foam	Ni foam	1 M KOH	400	72
NiFe LDH || Ni foam	Ni foam	1 M NaOH	470	59
NiMo HNRs || NiMo HNRs	Ti mesh	1 M KOH	410	73
$MoNi_4$ || $MoNi_4$	Ni foam	1 M KOH	350	74
Ni@N-graphene || Ni@N-graphene	Ni foam	1 M KOH	370	75
$NiCo_2S_4$@NiFe LDH || $NiCo_2S_4$@NiFe LDH	Ni foam	1 M KOH	370	76
NiFe-LDH-NS@DG || NiFe-LDH-NS@DG	Ni foam	1 M KOH	270	52
Pt/C || IrO_2	**Carbon paper**	**0.1 M KOH**	**390**	**This work**
PRN-550 || PRN-500	**Carbon paper**	**0.1 M KOH**	**300**	**This work**

References

1. G. Kresse and J. Hafner, *Phys. Rev. B*, 1993, **47**, 558-561.
2. G. Kresse and J. Hafner, *Phys. Rev. B*, 1994, **49**, 14251-14269.
3. G. Kresse and J. Furthmüller, *Phys. Rev. B*, 1996, **54**, 11169-11186.
4. G. Kresse and J. Furthmüller, *Comput. Mater. Sci.*, 1996, **6**, 15-50.
5. P. E. Blöchl, *Phys. Rev. B*, 1994, **50**, 17953-17979.
6. G. Kresse and D. Joubert, *Phys. Rev. B*, 1999, **59**, 1758-1775.
7. J. P. Perdew, K. Burke and M. Ernzerhof, *Phys. Rev. Lett.*, 1996, **77**, 3865-3868.
8. H. J. Monkhorst and J. D. Pack, *Phys. Rev. B*, 1976, **13**, 5188-5192.
9. J. K. Nørskov, T. Bligaard, A. Logadottir, J. R. Kitchin, J. G. Chen, S. Pandelov and U. Stimming, *J. Electrochem. Soc.*, 2005, **152**, J23.
10. G. Henkelman, A. Arnaldsson and H. Jónsson, *Comput. Mater. Sci.*, 2006, **36**, 354-360.
11. C. F. Dickens, J. H. Montoya, A. R. Kulkarni, M. Bajdich and J. K. Nørskov, *Surf. Sci.*, 2019, **681**, 122-129.
12. G. Henkelman, B. P. Uberuaga and H. Jónsson, *J. Chem. Phys.*, 2000, **113**, 9901-9904.
13. G. Henkelman and H. Jónsson, *J. Chem. Phys.*, 2000, **113**, 9978-9985.
14. M. A. G. Hevia, A. P. Amrute, T. Schmidt and J. Pérez-Ramírez, *J. Catal.*, 2010, **276**, 141-151.
15. S. Gaur, D. Pakhare, H. Wu, D. J. Haynes and J. J. Spivey, *Energy Fuels*, 2012, **26**, 1989-1998.
16. S. M. d. Lima and J. M. Assaf, *Mater. Res.*, 2002, **5**, 329-335.
17. J. Park, M. Risch, G. Nam, M. Park, T. J. Shin, S. Park, M. G. Kim, Y. Shao-Horn and J. Cho, *Energy Environ. Sci.*, 2017, **10**, 129-136.
18. M. Kim, H. Ju and J. Kim, *Appl. Catal. B: Environ.*, 2019, **245**, 29-39.
19. Y. Xu, S. Yin, C. Li, K. Deng, H. Xue, X. Li, H. Wang and L. Wang, *J. Mater. Chem. A*, 2018, **6**, 1376-1381.
20. H. Sivaram, D. Selvakumar, A. Alsalme, A. Alswieleh and R. Jayavel, *J. Alloys Compd.*, 2018, **731**, 55-63.
21. D. Wang, Q. Li, C. Han, Z. Xing and X. Yang, *ACS Cent. Sci.*, 2018, **4**, 112-119.
22. L. Zhu, S. Shan, V. Petkov, W. Hu, A. Kroner, J. Zheng, C. Yu, N. Zhang, Y. Li, R. Luque, C.-J. Zhong, H. Ye, Z. Yang and B. H. Chen, *J. Mater. Chem. A*, 2017, **5**, 7869-7875.
23. Y. Chen, B. deGlee, Y. Tang, Z. Wang, B. Zhao, Y. Wei, L. Zhang, S. Yoo, K. Pei, J. H. Kim, Y. Ding, P. Hu, F. F. Tao and M. Liu, *Nat. Energy*, 2018, **3**, 1042-1050.
24. Y. G. Choi, K. H. Kim, V. A. Chernov and J. Heo, *J. Non-Cryst. Solids*, 1999, **246**, 128-135.
25. J. Park, M. Park, G. Nam, M. G. Kim and J. Cho, *Nano Lett.*, 2017, **17**, 3974-3981.
26. Y. Zhou, Z. Wang, Z. Pan, L. Liu, J. Xi, X. Luo and Y. Shen, *Adv. Mater.*, 2019, **31**, 1806769.
27. Y. Tong, P. Chen, T. Zhou, K. Xu, W. Chu, C. Wu and Y. Xie, *Angew. Chem. Int. Ed.*, 2017, **56**, 7121-7125.
28. L. Fang, W. Li, Y. Guan, Y. Feng, H. Zhang, S. Wang and Y. Wang, *Adv. Funct. Mater.*, 2017, **27**, 1701008.
29. X. Han, X. Wu, Y. Deng, J. Liu, J. Lu, C. Zhong and W. Hu, *Adv. Energy Mater.*, 2018, **8**, 1800935.
30. M. Kim, H. Ju and J. Kim, *J. Mater. Chem. A*, 2018, **6**, 8523-8530.
31. M. Kim, H. Ju and J. Kim, *Chem. Eng. J.*, 2019, **358**, 11-19.
32. M. Gong, Y. Li, H. Wang, Y. Liang, J. Z. Wu, J. Zhou, J. Wang, T. Regier, F. Wei and H. Dai, *J. Am. Chem. Soc.*, 2013, **135**, 8452-8455.
33. J. Geng, L. Kuai, E. Kan, Q. Wang and B. Geng, *ChemSusChem*, 2015, **8**, 659-664.
34. C. Schwanke, H. S. Stein, L. Xi, K. Sliozberg, W. Schuhmann, A. Ludwig and K. M. Lange, *Sci. Rep.*, 2017, **7**, 44192.
35. N. Chandrasekaran and S. Muthusamy, *Langmuir*, *Binderless,* 2017, **33**, 2-10.
36. Z. Liu, C. Yu, X. Han, J. Yang, C. Zhao, H. Huang and J. Qiu, *ChemElectroChem*, 2016, **3**, 906-912.
37. X. Han, F. Cheng, T. Zhang, J. Yang, Y. Hu and J. Chen, *Adv. Mater.*, 2014, **26**, 2047-2051.
38. Y. Li, P. Hasin and Y. Wu, *Adv. Mater.*, 2010, **22**, 1926-1929.

39. Z. Peng, D. Jia, A. M. Al-Enizi, A. A. Elzatahry and G. Zheng, *Adv. Energy Mater.*, 2015, **5**, 1402031.
40. X. Ma, W. Zhang, Y. Deng, C. Zhong, W. Hu and X. Han, *Nanoscale*, 2018, **10**, 4816-4824.
41. M. Gao, W. Sheng, Z. Zhuang, Q. Fang, S. Gu, J. Jiang and Y. Yan, *J. Am. Chem. Soc.*, 2014, **136**, 7077-7084.
42. Q. Qin, H. Jang, P. Li, B. Yuan, X. Liu and J. Cho, *Adv. Energy Mater.*, 2019, **9**, 1803312.
43. F. Meng, H. Zhong, D. Bao, J. Yan and X. Zhang, *J. Am. Chem. Soc.*, 2016, **138**, 10226-10231.
44. D. A. Kuznetsov, M. A. Naeem, P. V. Kumar, P. M. Abdala, A. Fedorov and C. R. Müller, *J. Am. Chem. Soc.*, 2020, **142**, 7883-7888.
45. Q. Feng, Q. Wang, Z. Zhang, Y. Xiong, H. Li, Y. Yao, X.-Z. Yuan, M. C. Williams, M. Gu, H. Chen, H. Li and H. Wang, *Appl. Catal. B: Environ.*, 2019, **244**, 494-501.
46. D. J. Payne, R. G. Egdell, D. S. L. Law, P.-A. Glans, T. Learmonth, K. E. Smith, J. Guo, A. Walsh and G. W. Watson, *J. Mater. Chem.*, 2007, **17**, 267-277.
47. C. Du, L. Yang, F. Yang, G. Cheng and W. Luo, *ACS Catal.*, 2017, **7**, 4131-4137.
48. Y. Zhu, J. Dai, W. Zhou, Y. Zhong, H. Wang and Z. Shao, *J. Mater. Chem. A*, 2018, **6**, 13582-13587.
49. M. Ledendecker, S. Krick Calderón, C. Papp, H.-P. Steinrück, M. Antonietti and M. Shalom, *Angew. Chem. Int. Ed.*, 2015, **54**, 12361-12365.
50. H. B. Wu, B. Y. Xia, L. Yu, X.-Y. Yu and X. W. Lou, *Nat. Commun.*, 2015, **6**, 6512.
51. H. Vrubel and X. Hu, *Angew. Chem. Int. Ed.*, 2012, **51**, 12703-12706.
52. Y. Jia, L. Zhang, G. Gao, H. Chen, B. Wang, J. Zhou, M. T. Soo, M. Hong, X. Yan, G. Qian, J. Zou, A. Du and X. Yao, *Adv. Mater.*, 2017, **29**, 1700017.
53. C. Tang, R. Zhang, W. Lu, L. He, X. Jiang, A. M. Asiri and X. Sun, *Adv. Mater.*, 2017, **29**, 1602441.
54. Y. Xu, Y. Li, S. Yin, H. Yu, H. Xue, X. Li, H. Wang and L. Wang, *Nanotechnology*, 2018, **29**, 225403.
55. X. Wu, X. Han, X. Ma, W. Zhang, Y. Deng, C. Zhong and W. Hu, *ACS Appl. Mater. Interfaces*, 2017, **9**, 12574-12583.
56. J. Tian, Q. Liu, A. M. Asiri and X. Sun, *J. Am. Chem. Soc.*, 2014, **136**, 7587-7590.
57. J. Su, Y. Yang, G. Xia, J. Chen, P. Jiang and Q. Chen, *Nat. Commun.*, 2017, **8**, 14969.
58. Z. Xing, C. Han, D. Wang, Q. Li and X. Yang, *ACS Catal.*, 2017, **7**, 7131-7135.
59. J. Luo, J.-H. Im, M. T. Mayer, M. Schreier, M. K. Nazeeruddin, N.-G. Park, S. D. Tilley, H. J. Fan and M. Grätzel, *Science*, 2014, **345**, 1593-1596.
60. H. Liang, L. Li, F. Meng, L. Dang, J. Zhuo, A. Forticaux, Z. Wang and S. Jin, *Chem. Mater.*, 2015, **27**, 5702-5711.
61. L. Yu, H. Zhou, J. Sun, F. Qin, F. Yu, J. Bao, Y. Yu, S. Chen and Z. Ren, *Energy Environ. Sci.*, 2017, **10**, 1820-1827.
62. Y. Wang, L. Chen, X. Yu, Y. Wang and G. Zheng, *Adv. Energy Mater.*, 2017, **7**, 1601390.
63. L.-A. Stern, L. Feng, F. Song and X. Hu, *Energy Environ. Sci.*, 2015, **8**, 2347-2351.
64. M. Pozzo, G. Carlini, R. Rosei and D. Alfè, *J. Chem. Phys.*, 2007, **126**, 164706.
65. J. L. C. Fajín, M. N. D. S. Cordeiro, F. Illas and J. R. B. Gomes, *J. Catal.*, 2010, **276**, 92-100.
66. R. C. Catapan, A. A. M. Oliveira, Y. Chen and D. G. Vlachos, *J. Phys. Chem. C*, 2012, **116**, 20281-20291.
67. D. W. Blaylock, T. Ogura, W. H. Green and G. J. O. Beran, *J. Phys. Chem. C*, 2009, **113**, 4898-4908.
68. H. Seenivasan and A. K. Tiwari, *J. Chem. Phys.*, 2013, **139**, 174707.
69. A. Mohsenzadeh, K. Bolton and T. Richards, *Surf. Sci.*, 2014, **627**, 1-10.
70. N. Jiang, B. You, M. Sheng and Y. Sun, *Angew. Chem. Int. Ed.*, 2015, **54**, 6251-6254.
71. A.-L. Wang, H. Xu and G.-R. Li, *ACS Energy Lett.*, 2016, **1**, 445-453.
72. C. Tang, N. Cheng, Z. Pu, W. Xing and X. Sun, *Angew. Chem. Int. Ed.*, 2015, **54**, 9351-9355.
73. J. Tian, N. Cheng, Q. Liu, X. Sun, Y. He and A. M. Asiri, *J. Mater. Chem. A*, 2015, **3**, 20056-20059.
74. Y. Jin, X. Yue, C. Shu, S. Huang and P. K. Shen, *J. Mater. Chem. A*, 2017, **5**, 2508-2513.
75. Y. Xu, W. Tu, B. Zhang, S. Yin, Y. Huang, M. Kraft and R. Xu, *Adv. Mater.*, 2017, **29**, 1605957.

76. J. Liu, J. Wang, B. Zhang, Y. Ruan, L. Lv, X. Ji, K. Xu, L. Miao and J. Jiang, *ACS Appl. Mater. Interfaces*, 2017, **9**, 15364-15372.